CO_2 methanation over alumina-supported cobalt oxide and carbide synthesized by reverse microemulsion method

by

Yue Yu

A thesis

presented to the University of Waterloo

in fulfillment of the

thesis requirement for the degree of

Master of Applied Science

in

Chemical Engineering

Waterloo, Ontario, Canada, 2019

AUTHOR’s DECLARATION

I hereby declare that I am the sole author of this thesis. This is a true copy of the thesis, including any required final revisions, as accepted by my examiners.

I understand that my thesis may be made electronically available to the public.

Abstract

In the past age, CO_2 conversion catalysts have gained attention due to various environmental issues caused by CO_2 emission. Catalytic reduction of CO_2 using renewable hydrogen as reductant to produce renewable fuels is considered as a potential solution to store the surplus renewable energy and reduce the CO_2 emission. Alumina-supported cobalt oxide and cobalt carbide catalysts prepared by reverse microemulsion (RME) method were investigated for CO_2 methanation. Results showed that the prepared catalysts were nanosized particles ranged from 5-15 nm. XRD, BET, SEM and TEM were used for catalysts characterization and TPR was conducted to study the reducibility.

The catalytic performance of these catalysts was studied by CO_2 methanation reaction. At 400 °C, 3 bar, under a 60,000 mL g_{cat}^{-1} h^{-1} flow (H_2:CO_2=4:1), the selectivity to methane on alumina-supported cobalt carbide catalysts can reach 0.96 and the conversion of CO_2 was 0.78, showing high catalytic activity and mild reaction condition. With increasing pressure, the conversion of CO_2, as well as the selectivity to CH_4 both increased and reached 0.91 and 0.98 respectively at 11 bar showing excellent performance towards CO_2 methanation.

In-situ FTIR was used to study the mechanism of the reaction on alumina-supported cobalt catalysts. The pathway from CO_2 to methane and adsorbed intermediates on catalysts were investigated. Intermediates and adsorbed species on the catalysts were investigated during the reaction. At lower temperature and lower gas concentration, CO_2 was adsorbed on the surface as carbonates. When the reaction condition was achieved, adsorbed CO_2 started to be reacted to CO and CH_4 and intermediate species started to appear.

Keywords: CO_2 methanation, alumina supported cobalt carbide, reverse microemulsion

Acknowledgment

I would like to thank my supervisor Professor David Simakov and Professor Aiping Yu for the continuous support and patient guidance during my program.

I would also like to thank my committee numbers: Professor Yuning Li, Professor Xianshe Feng for their precious comments and suggestions on my project.

This work would not have been possible without the help and advice from Yichen Zhuang, Guanjie Sun, Sogol Tabar, Muhammad Waqas and Robert Currie.

I would also like to acknowledge the support of the Waterloo Institute of Sustainable Energy (WISE), the Ontario Centers of Excellence (OCE), the Canada Foundation for Innovation (CFI), and the Natural Science and Engineering Research Council (NSERC).

Finally yet importantly, I would like to thank my dear parents and friends for their support and encouragement.

Table of Content

AUTHOR's DECLARATION ii
Abstract iii
Acknowledgment iv
Table of Content v
List of Figures vii
List of Tables ix
Nomenclature x
Chapter 1: Introduction 1
1.1 Problem Statement 1
1.2 Project objective 2
1.3 Thesis outline 2
Chapter 2: Background 4
2.1 Global warming and CO_2 emission 4
2.2 Power to gas (PtG) 5
2.3 Thermo-catalytic conversion of CO_2 7
2.3.1 CO_2 methanation 8
2.3.2 Reverse water gas shift and other side reactions 9
2.4 CO_2 methanation catalysts 9
2.4.1 Noble metal catalysts 10
2.4.2 Transition metal catalysts 11
2.5 Reverse micro-emulsion (RME) method for catalysts preparation. 14
Chapter 3 Methodology 17
3.1 X-ray powder diffraction 17
3.2 ICP-EOS 18
3.3 Temperature-programmed reduction (TPR) 19
3.4 Surface area analysis (SAA) 20
3.5 Scanning Electron Microscope (SEM) and Scanning Electron Microscope – Energy dispersive X-ray spectroscope (SEM-EDS) 21
3.6 Transmission electron microscopy (TEM) 22
3.7 Thermogravimetric Analysis (TGA) 22
3.8 FTIR 23

3.8.1 In-situ FTIR 23
3.8.2 IR detector for catalytic performance evaluation 24
Chapter 4 Experiment Setup 25
4.1 Catalysts synthesis 25
4.1.1 CoO_x/Al_2O_3 and CoC_x/Al_2O_3 by reverse microemulsion method 25
4.1.2 Reference catalysts 28
4.2 Catalysts characterization 28
4.3 Flow system setup 29
4.4 Catalytic performance evaluation 30
3.5 In-situ FTIR study 31
Chapter 5 Results and discussion 33
5.1 Characterization 33
5.2 Catalytic performance evaluation 40
5.3 In-situ FTIR study 45
Chapter 6 Conclusion and future work 48
6.1 Conclusion 48
6.2 Future work 49
Reference 50

List of Figures

Fig. 1 Canada's 2015 natural gas usage percentage by sector [10]. 5

Fig. 2 Sankey diagram of the PtG Process efficiency [5]. 6

Fig. 3 Reaction pathways of producing synthetic fuels and chemicals via thermo-catalytic CO_2 conversion [3]. 7

Fig. 4 Common trends of the conversion and selectivity as a function of temperature and pressure [13]..... 9

Fig. 5 CO_2 conversion and selectivity to CH_4 with different Ni loadings. 12

Fig. 6 Catalytic performance of Co doped NiO/Al_2O_3 catalyst (10N3COMA), NiO/Al_2O_3 catalysts (10NOMA) and Co_3O_4/Al_2O_3 catalysts (3COMA). 13

Fig. 7 RME nano-droplets and reaction sketch [4]. 14

Fig. 8 Conversion of methane in combustion process on catalysts prepared via different methods. a, sol-gel-derived conventional BHA; b, reverse-microemulsion-derived BHA nanoparticles; c, reverse-microemulsion-derived CeO_2-BHA nanocomposite. GHSV=60,000 h^{-1}, 1% methane in air. 15

Fig. 9 Bragg's law schematic. 17

Fig. 10 ICP-OES schematic diagram. 18

Fig. 11 TPR schematic diagram. 19

Fig. 12 SEM Schematic [1]..... 21

Fig. 13 TEM Schematic [2]. 21

Fig. 14 in-situ FTIR schematic diagram. 23

Fig. 15 Cobalt catalysts preparation procedure by RME method. 25

Fig. 16 RME preparation procedure. 26

Fig. 17 CoOx and CoCx preparation procedure. 27

Fig. 18 Flow system setup. 29

Fig. 19 CO and CO_2 profile during carburization process. Heating rate = 2 °C/min. 33

Fig. 20 XRD patterns of CoOx and CoCx. 35

Fig. 21 TPR patterns of fresh CoOx and CoCx. Catalysts were pre-treated in argon at 150 °C for 30 min. Heating rate = 10 °C /min. 36

Fig. 22 SEM micrographs of fresh CoO_x and CoCx 38

Fig. 23 SEM-EDS mapping of CoC_x-A. 39

Fig. 24 TEM micrographs of supported catalysts 40

Fig. 25 Catalytic performance of CoO_x and CoC_x prepared by RME method at different temperature. 41

Fig. 26 Comparisons of catalysts prepared by RME and wet impregnation. 42

Fig. 27 Catalyst performance of CoC_x-B at different pressure.. 43

Fig. 28 TGA-FTIR analysis for spent catalysts. 44

Fig. 29 In-situ FTIR spectra as a function of temperature of CoO_x samples, after 15min reaction under 2% CO_2 /8%H_2/Ar. 45

Fig. 30 In-situ FTIR spectra as a function of time of CoO_x samples, at 350 °C under 2% CO_2 /8%H_2/Ar 46

Fig. 31 In-situ FTIR spectra as a function of temperature of CoC_x samples, after 15min reaction under 2% CO_2 /8%H_2/Ar. 47

List of Tables

Table. 1 Comparison of Pd-Mg/SiO_2 catalysts prepared by different methods ……...11

Table. 2 Characteristic of fresh catalysts ……...……26

Nomenclature

λ	wavelength of the X-ray
n	any positive integer
d	plane spacing
θ	the grazing angle
p	the pressure at equilibrium
p_2	the saturated vapor pressure of the adsorbed gas
Vm	the volume of gas required to form a monolayer on the surface
V	the amount of adsorption
C	constant
NA	Avogadro constant
s	adsorption cross-sectional area of the adsorbed species
V	molar volume of the adsorbed species
a	quality of the adsorbent material.
f1	CO2 conversion to CO
f_2	CO_2 conversion to CH_4
$F_{C,out}$	total outlet molar flow rate of carbon-containing species
$F_{H_2,f}$	feed molar flow rate of H_2
$F_{CO_2,f}$	feed molar flow rate of CO_2
$F_{CO,out}$	outlet molar flow rate of CO
$F_{CH_4,out}$	outlet molar flow rate of CH_4
$F_{t,out}$	total outlet molar flow rate
Q_f	volumetric feed flow rate
S_{CH_4}	selectivity to CH_4
W_c	catalyst weight
X_{CO_2}	CO_2 conversion

y_i	mole fraction (i stands for either CO_2, CO, or CH_4)
ΔH°_{298}	reaction enthalpy
α	H_2:CO_2 ratio in the feed

Abbreviations

CB	carbon balance
GHSV	gas hourly space velocity
GHG	greenhouse gas
PtG	power to gas
RWGS	reverse water gas shift

Chapter 1: Introduction

1.1 Problem Statement

Since the Industrial Revolution, fossil fuel has played an essential role in our daily life. The amount of fossil fuel use has increased rapidly. Because of this, the concentration of CO_2 and other greenhouse gases in the atmosphere has reached a new level due to exhaust emissions generated by human activity. More heat radiation from the earth's surface is absorbed by the atmosphere instead of radiating to space, and this phenomenon will cause global warming. To this day, we still cannot offer an efficient solution to the problem, but we can mitigate the greenhouse effect by reducing greenhouse gas emissions.

Reducing the greenhouse gas emission is gradually becoming a necessary mission for every country and area. Ontario has met its target of 2014: to decrease 6% of the greenhouse emission compare with 1990 level[6]. This target was achieved by closing fossil fuel power plants all over Ontario and around 60% of the electricity in Ontario is generated by nuclear now[7]. The next goal for Ontario is to achieve 15% below 1990 by 2020, which is a big jump. To close some of this gap, there are still a lot of works to be done.

If we can transfer CO_2 to synthetic fuels and chemicals and introduce the synthetic fuel into the existing energy system, the value of CO_2 can be used entirely, and the emission can be reduced. CO_2 methanation, also known as Sabatier reaction, is attracting increasing attention currently. Conversion of CO_2 to methane not only consumes the CO_2, which is otherwise emitted (or stored) but also produces valuable fuels that can be simply injected to the current energy grid. The energy of renewable electricity can be stored in the form of chemical energy inside the

chemical bonds. CO_2 utilization via power to gas can be a solution for the increasingly serious situation of global warming caused by greenhouse gases emission.

The hydrogen required in CO_2 methanation can be generated from the electrolysis of water. One key point of the CO_2 conversion is that, the energy, or the hydrogen required in the reaction should not be generated from a high carbon footprint process. If the electricity for water electrolysis is from a fossil fuel based power plant, the carbon footprint of the methanation will be positive and it is meaningless to convert the CO_2.

1.2 Project objective

In this project, the objective is to investigate several cobalt-based catalysts for CO_2 methanation. Aim catalysts need to be suitable for industrial production, while having high activity and high selectivity towards CH_4. To achieve these requirements, aim catalysts should have porous morphology and high surface area to give enough active site for the reaction. To understand the pathway of the methanation process, the mechanism also needs to be determined.

Catalysts were prepared by reverse micro-emulsion (RME) method first and then characterized by several characterization technologies to understand the structure and morphology. The CO_2 conversion and selectivity to CH_4 were tested on the catalysts in a range of different temperature and pressure to search for the optimum reaction condition. Mechanism of the reaction in molecular level was investigated by in-situ FTIR study.

1.3 Thesis outline

Chapter 2 includes a general review of the CO_2 emission issue in Ontario as well as worldwide. The idea of power to gas (PtG) is introduced. Different catalysts introduction for CO_2

methanation and reverse water gas shift are also summarized in Chapter 2 in terms of groups of elements.

Chapter 3 and Chapter 4 gives the methodology of the experiments including catalysts preparation by RME method and wet impregnation method for reference catalysts, characterization method including X-ray powder diffraction (XRD), temperature-programmed reduction (TPR), surface area analysis (SAA), Scanning electron microscope (SEM) and transmission electron microscopy (TEM), flow system setup for catalytic performance test and in-situ FTIR setup for mechanism study.

Results and discussion are carried out in Chapter 5, which is divided into three separate part: characterization, performance and in-situ FTIR study. Catalysts structure, morphology, and reducibility are obtained from characterization studies. Conversion of CO_2 and selectivity to CH_4 are tested through catalytic performance test in a range of temperature and pressure. In-situ FTIR study towards CO_2 methanation is also included in Chapter 5.

According to the results showed in Chapter 5, conclusion and future work are presented in Chapter 6. During the project processing, potential improvement of the catalysts on preparation method and catalyst components were raised, providing possible research directions.

Chapter 2: Background

2.1 Global warming and CO_2 emission

The atmosphere is like the glass over a greenhouse to keep inside warm so that the temperature will not drop dramatically in the night. Solar radiation is mainly short-wave radiation, while the radiation back from the earth surface to the atmosphere is long-wave radiation. The cause of global warming is complicated. However, it can be divided into two aspects, the natural climate fluctuation and human activities. The former includes the change of solar radiation, change of earth orbit and self-monitoring of the global climate system. The latter includes the overuse of fossil fuel, deforestation, emission cause from industrial and agricultural, forests and land use change, etc.

However, there is an increasing number of evidences showing that the main reason of global warming is the rising concentration of greenhouse gas in the atmosphere, which is caused by human activity, primarily industrial and agriculture. Therefore, the accentuation of the greenhouse effect is the most possible cause of global warming. The consequences of global warming and climate change can be disastrous. According to the World Meteorological Organization [8], the average temperature of global surface continues to rise since recoded from 1861. During the 21st century, the temperature is likely to rise by 0.3 to 1.7 °C. The prediction made by the Intergovernmental Panel on Climate Change in 1995 said that if emissions of greenhouse gases were not reduced in the next decades, the global average temperature would increase 0.2 °C per decade. The tiny number changing seems like it will not cause a severe consequence to our life, but if the temperature continues to increase, the rise of sea level due to melting glaciers will cause 1400 cities in the US submerged underwater in 2100.

As of May 2013, CO_2 concentrations in the Earth's atmosphere were once more than 400 ppm (400 ppm or 0.04%) [9]. Though the increase of carbon dioxide is beneficial to the generation of photosynthetic products of green plants, it also causes the change of degree and precipitation by influencing the energy balance of the earth, which will have a negative effect on climate productive potentialities. Carbon dioxide plays a significant role in global warming, because of this, the countermeasure to mitigate global warming is mainly focus on reducing the emission of carbon dioxide.

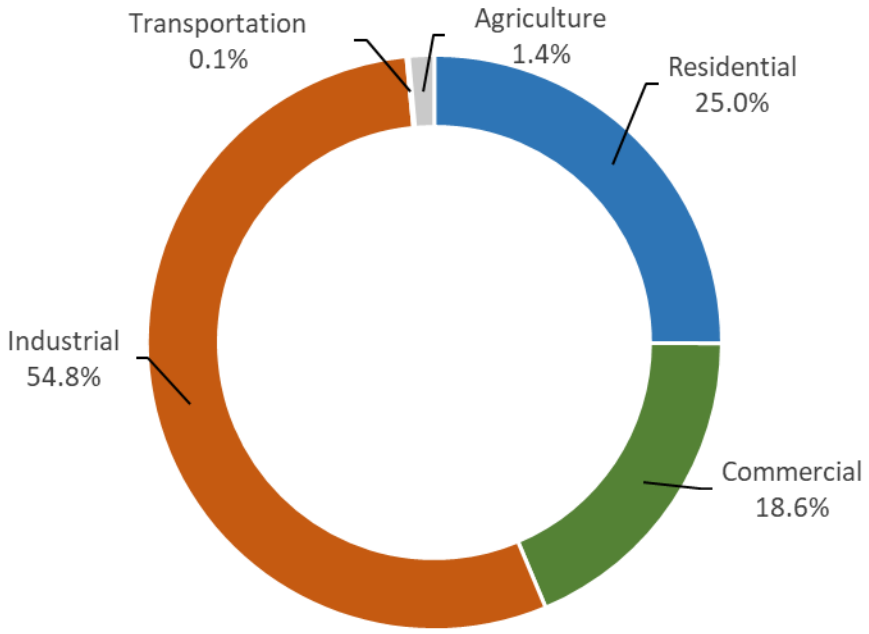

Fig. 1 Canada's 2015 natural gas usage percentage by sector [10].

2.2 Power to gas (PtG)

In Ontario, 80% of our energy source is still from fossil fuel and methane is widely used in residential heating and other purposes. In 2015, the total usage of methane in Canada was 2,754 petajoules (PJ). There are still many industries need methane as raw material or energy source.

More than half of the methane utilized in Canada was for industrial production, as described in **Fig. 1**. [10]

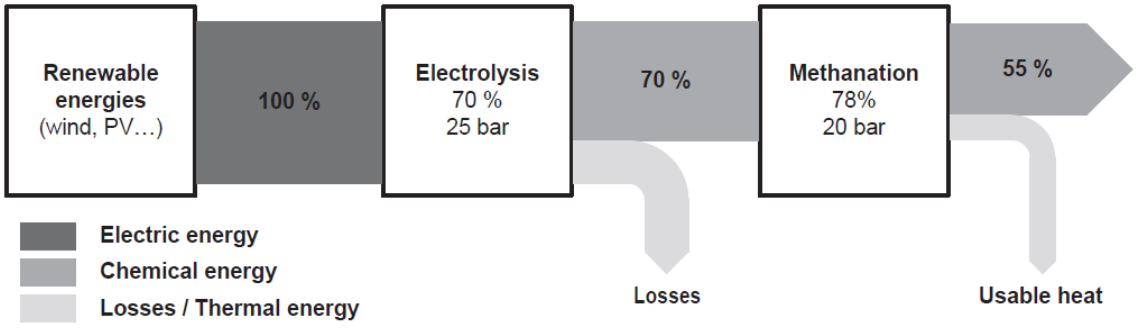

Fig. 2 Sankey diagram of the PtG Process efficiency [5].

With the increasing number of renewable energies developed all around the world, the utility of surplus electricity is significant, since most of the renewable energy sources, such as wind and hydro, are fluctuating and intermittent. Power to gas (PtG) is a promising way to store the electricity in the form of chemical energy inside chemical bond and methane is the most favoured product since the consumption of methane is massive in many industries currently and the existing methane grid allows the convenience of utilization. The idea is to reduce CO or CO_2 to methane and inject the generated methane to the present methane grid. In Germany, Audi has the biggest power to gas plant operated from 2013, Audi e-gas plant, where the CO_2 is from a biogas plant, hydrogen required is from three alkaline electrolysers. [11]

A disadvantage that needs to be eliminated in the PtG chain is the efficiency of water electrolysis and the efficiency of methanation as demonstrated in **Fig. 2**. [5] The total energy will lose 30% from renewable electricity to compressed hydrogen delivered from the electrolysis. Currently, there are three promising electrolysis methods, which are alkaline electrolysis, PEM

electrolysis, and solid oxide electrolysis. Comparing the economic numbers, alkaline electrolysis is the most favoured one for now, but if the cost of PEM electrolysis can be reduced in the future, it will be the most suitable one for flexible industrial production. In **Fig. 2**, the efficiency is considered for current available electrolysis technologies (AEL and PEM). Another link in the process that requires potential development is methanation process. The efficiency is limited by the equilibrium of the reaction but the energy that is released in the form of heat can be utilized as a heat source for other processes [5].

2.3 Thermo-catalytic conversion of CO_2

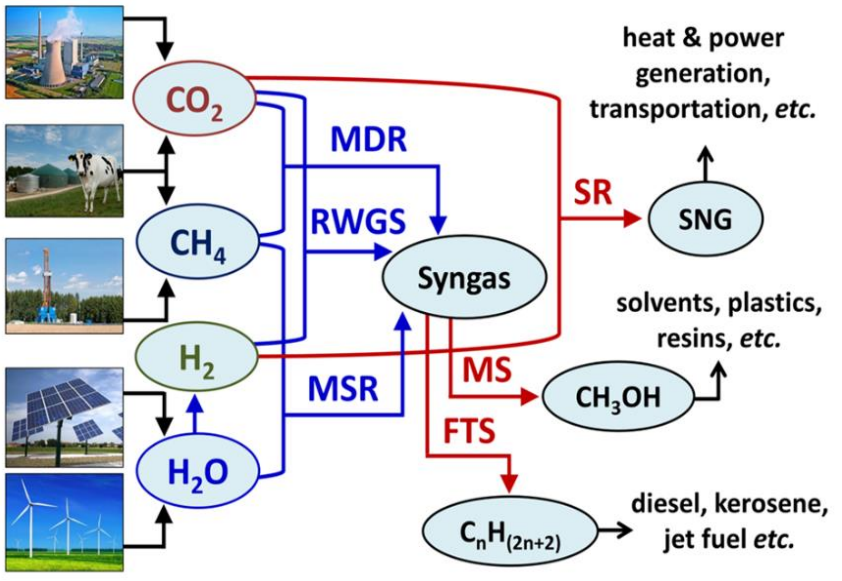

Fig. 3 Reaction pathways of producing synthetic fuels and chemicals via thermo-catalytic CO_2 conversion [3].

Usually, there are three pathways of CO_2 reduction: thermal-catalytic reduction, photochemical reduction and electrochemical reduction. Photochemical reduction and electrochemical reduction have their own limitation of efficiency and capacity. However, thermo-catalytic conversion of CO_2 is favoured by its high temperature reaction condition that provides

high reaction rate and allows large volume production. There is a sketch of variety thermo-catalytic CO_2 conversion pathways (**Fig. 3**). Using CO_2 and H_2 as reactants, syngas can be generated via methane dry reforming reaction (MDR) and reverse water gas shift reaction (RWGS) and can be further transformed to other valuable chemicals. Another product that can be produced by CO_2 is methane. Via CO_2 methanation, also known as Sabatier reaction, CO_2 can be converted to methane and methane is a good energy source for lots of industries and also a suitable fuel for home heating.

2.3.1 CO_2 methanation

CO_2 methanation, also called Sabatier reaction is an extremely exothermic reaction. The conversion to CH_4 is favoured at relatively low temperature and high pressure. The best performance of the catalysts is often obtained at 350 °C. The reaction is usually carried out through a fixed bed reactor on metal-based catalysts. Since the methanation reaction, **eq. (1)** [12], is highly exothermic, removing heat from the system to maintain the optimal reaction temperature is one big challenge of the reaction design. Currently, two pathways of the reaction are believed mostly, one is the CO_2 molecules are adsorbed on the catalyst surface and dissociated to CO followed by reaction with H_2 while the other mechanism does not involve CO and the adsorbed CO_2 is directly transferred to CH_4.

$$CO_2 + 4\,H_2 \rightleftharpoons CH_4 + 2\,H_2O \qquad \Delta H^{\circ}_{298} = -164.9\ kJ/mol \qquad (1)$$

$$CO + 3\,H_2 \rightleftharpoons CH_4 + H_2O \qquad \Delta H^{\circ}_{298} = -206.1\ kJ/mol \qquad (2)$$

$$CO_2 + H_2 \rightleftharpoons CO + H_2O \qquad \Delta H^{\circ}_{298} = +41\ kJ/mol \qquad (3)$$

$$2\,CO + 2\,H_2 \rightleftharpoons CO_2 + CH_4 \qquad \Delta H^{\circ}_{298} = -247 kJ/mol \qquad (4)$$

$$2\,CO \rightleftharpoons C + CO_2 \qquad \Delta H^{\circ}_{298} = -172\ kJ/mol \qquad (5)$$

$$CO + H_2 \rightleftharpoons C + H_2O \qquad \Delta H^{\circ}_{298} = -131\ kJ/mol \qquad (6)$$

$$CO_2 + 2\,H_2 \rightleftharpoons C + 2\,H_2O \qquad \Delta H^{\circ}_{298} = -90\ kJ/mol \qquad (7)$$

2.3.2 Reverse water gas shift and other side reactions

The CO_2 methanation is always accompanied by the reverse water gas shift **eq. (2)**, the methanation of CO **eq. (3)** and reverse dry reforming **eq. (4).** The selectivity of each reaction is highly depended on the catalysts' category and the support materials. CO_2 will be adsorbed on the catalysts surface differently which will lead to varies of intermediates and reaction pathways. **eq. (5)** to **eq. (7)** is the main reason for the deposition carbon formation during catalysts degradation that will block the pores on the surface and decrease the surface area which is related to the activity of the catalysts. However, the fouling catalysts caused by carbon can be regenerated by combustion and oxidation at a suitable condition.

2.4 CO_2 methanation catalysts

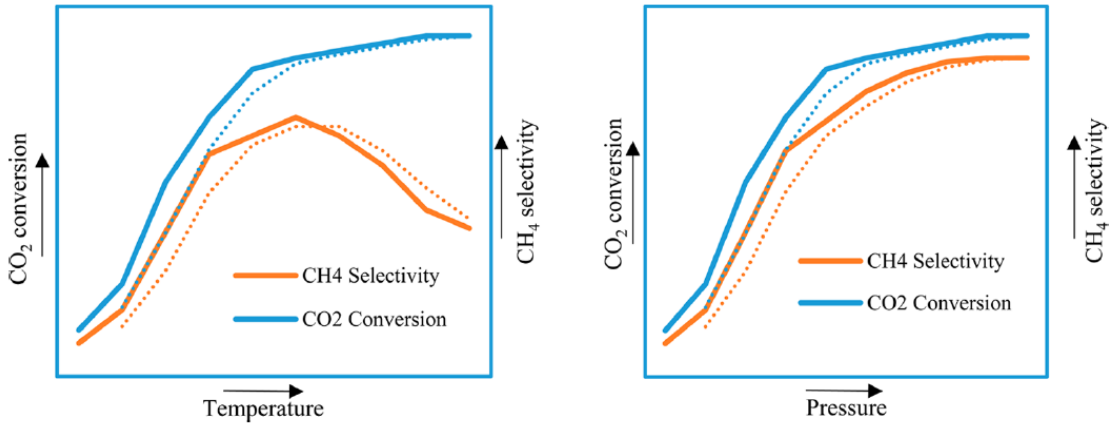

Fig. 4 Common trends of the conversion and selectivity as a function of temperature and pressure [13].

Metal catalysts mainly from VIII – XI group of the periodic table have been confirmed on CO_2 methanation. Catalytic activity and CH_4 selectivity are two important factors to evaluate the

performance. During decades of investigation, the activity of the metals that can be employed in methanation can be ranked as: Ru > Rh > Ni > Fe > Co > Os > Pt > Ir > Mo > Pd > Ag > Au, while the selectivity to CH_4 can be ranked as follow: Pd > Pt > Ir > Ni > Rh > Co > Fe > Ru > Mo > Ag > Au. [13]

There is a common trend that with the increasing of the temperature, the total conversion of CO_2 will increase, while the selectivity to methane will decline, as shown in **Fig. 4**. The actual number of conversion and selectivity may vary for different catalysts (solid line and dash line), but the variation trend is the same. This is reasonable since the methanation reaction is exothermic and the reverse water gas shift is endothermic. With the increasing pressure, the CO_2 conversion and CH_4 selectivity will both increase because the total gas phase molecules will decrease during the reaction.

2.4.1 Noble metal catalysts

Rhodium is the most developed noble material for CO_2 methanation. With the promotion of alumina support, CO_2 molecules can be adsorbed on the Rhodium catalysts surface and dissociated to CO and O. If the support can be switched to TiO_2, the most active catalyst among Rhodium catalysts will be obtained which may due to the interaction between the metal and the support [14] [15]. However, the cost of the TiO_2 support is much higher than the alumina support.

Ruthenium was reported to be the most active material [16], but the performance is sensitive to the dispersion and the particle size determined by the preparation method. Wet impregnation method is not suitable for controlling the resulting catalysts, therefore, a dry synthesis procedure called polyhedral barrel sputtering was offered in order to control the particle size and the dispersibility [17]. The support of the Ru catalysts will also affect the activity. A series

of support materials have been studied and TiO_2 support still showed superior advantages same as on Rhodium.

Palladium was also investigated as a methanation catalyst and the combination with Mg will improve the selectivity towards CH_4 and allow hydrogen to dissociate on the surface. Park et al., prepared size controlled Pd-Mg/SiO2 catalysts via reverse microemulsion and the obtained 95% selectivity to methane with 59% CO_2 conversion. Compare to the Pd-Mg/SiO_2 catalysts prepared by conventional wet impregnation, the conversion of CO_2 and selectivity to CH_4 are both increased substantially as showed in Table *1* [18]. However, the utilization of most noble metal catalysts are limited by the high price. [19]

Table 1 Comparison of Pd-Mg/SiO_2 catalysts prepared by different methods [18].

	CO_2 conversion (%)	H_2 conversion (%)	CH_4 Selectivity (%)	CH_4 Yield (%)
Pd(RME)/SiO_2	40.8	11.4	10.4	4.3
Pd(Imp)/SiO_2	40.6	9.6	6.5	2.6
Mg(RME)/SiO_2	0.8	6.7	10.3	0.1
Pd-Mg(RME)/SiO_2	59.2	26.9	95.3	56.4
Mg(Imp)/Pd/SiO_2	40	15.3	76.2	30.4

2.4.2 Transition metal catalysts

Nickel is the most investigated elements in the past decades. Studies have been carried out for different support and doping elements. Because of the low price and abundance, nickel is widely employed in industrial production but the sintering effect during reaction restricted the utilization [19] [20]. The performance of the nickel catalysts is highly depended on the support materials and the promoters. The influences of nickel loading on Al_2O_3 supported catalysts was studied by Rahmani et, al [21]. Increasing the loading of nickel will give more active component but the surface area that can provide active sites will decrease as shown in **Fig. 5**. The best

performance is reached when the loading is 20 wt%. Liu [22], reported the addition of ceria will enhance the stability of the catalyst and also the CO_2 conversion. After 120 hours, the conversion of CO_2 decreased slightly from 78.5% to 74.3% at 350 °C. Adding another metal as doping metal will affect the interaction behavior between the metal and the support. Adding W to the Ni-Mg catalysts can change the surface structure and the active sites, which is strongly associated to the catalytic performance, furthermore enhance the stability and reactivity of the nickel catalysts [23]. Nickel catalysts supported on silica is also studied. Nickel supported on MCM-41 catalysts was reported to have a high selectivity to CH_4. A selectivity of 96.1% to methane was achieved on 3% nickel supported on MCM-41 with a 16.8% CO_2 conversion [24]. However, during the reaction, nickel carbonyl, which is a toxic compound that can harm the human organism, can be generated, which should also be considered.

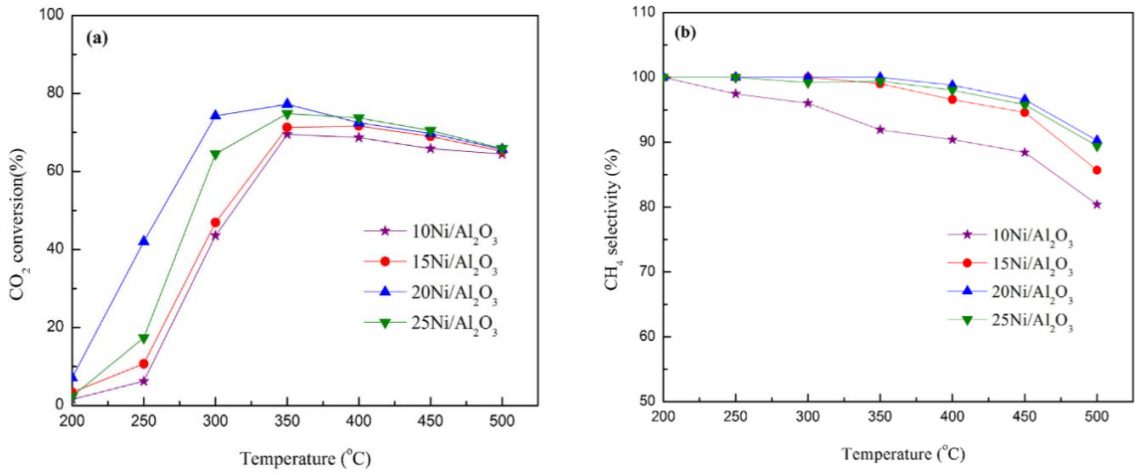

Fig. 5 CO_2 conversion and selectivity to CH_4 with different Ni loadings.

Reaction conditions: GHSV =9000 mL g_{cat}^{-1} h^{-1}, H_2/CO_2 molar ratio= 3.5.

Iron is reported to have similar activity as nickel but the selectivity to CO_2 methanation is lower, so Fe is mostly used in Fischer-Tropsch reaction. Cobalt has not attracted much attention in CO_2 methanation because the price is higher than nickel and the performance reported did not

show advantages. However, cobalt can be used as a promoter and doped on nickel [25]. In **Fig. 6**, the addition of cobalt on NiO/Al_2O_3 catalyst improved the catalytic performance and the conversion is higher than NiO/Al_2O_3 and Co_3O_4/Al_2O_3. Ni, Fe and Co are all easy to be oxidized in the atmosphere other than the noble metals. [13] [26]

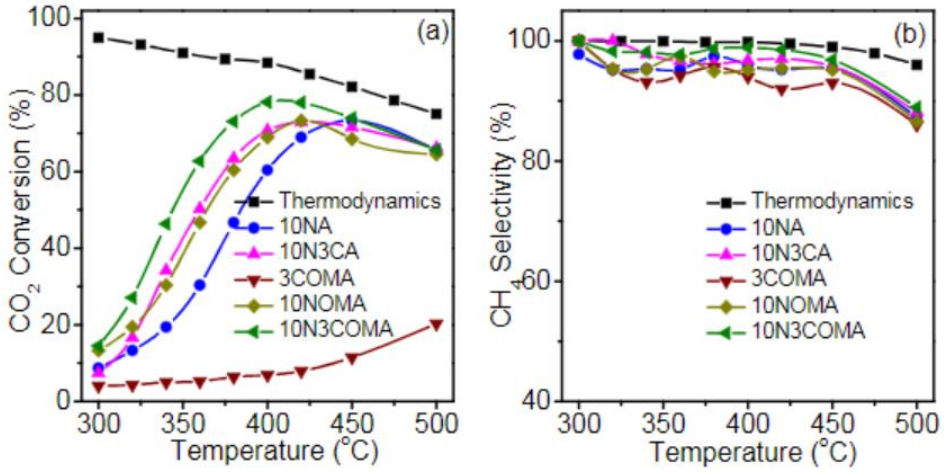

Fig. 6 Catalytic performance of Co doped NiO/Al_2O_3 catalyst (10N3COMA), NiO/Al_2O_3 catalysts (10NOMA) and Co_3O_4/Al_2O_3 catalysts (3COMA).

2.5 Reverse micro-emulsion (RME) method for catalysts preparation.

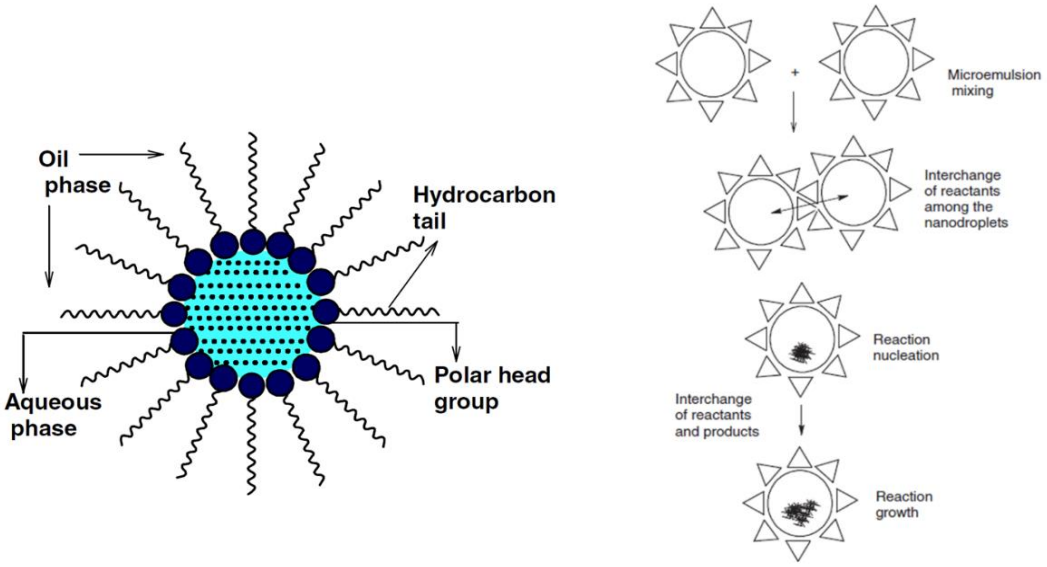

Fig. 7 RME nano-droplets and reaction sketch [4].

In order to obtain a suitable catalyst for methanation, the required catalyst needs to have a series of advantages. The catalysts should be active, stable and have good selectivity towards CO_2 methanation. The activity of the thermo-catalysts is highly related to the particle size, dispersibility and the surface area. High surface area will provide a large number of active sites and results in high reaction rate. Since the surface area per weight unit is usually increased with smaller particle size, reducing the particle size is one of the significant objectives in catalysts development. There were plenty of studies aimed at innovative synthesis procedures of the catalysts that can control the particle size in the desired range.

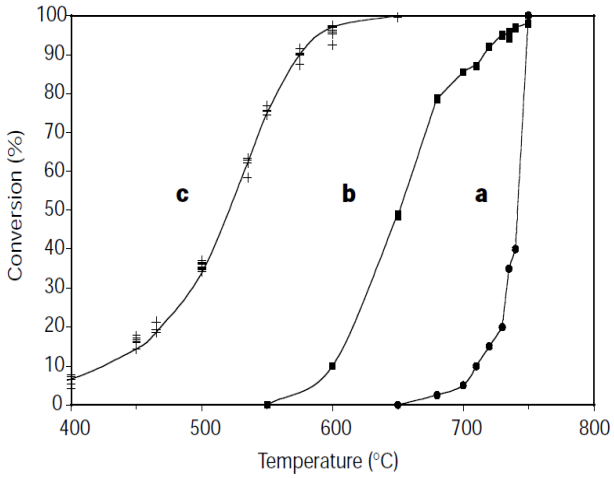

Fig. 8 Conversion of methane in combustion process on catalysts prepared via different methods. a, sol-gel-derived conventional BHA; b, reverse-microemulsion-derived BHA nanoparticles; c, reverse-microemulsion-derived CeO_2-BHA nanocomposite. GHSV=60,000 h^{-1}, 1% methane in air.

Reverse microemulsion was first proposed by Schulman, 1959. A typical water in oil reverse microemulsion system is shown in **Fig. 7** [4]. Aqueous phase was surrounded by surfactant molecules and oil is the continuous phase. The polar head groups of the surfactant molecules are attracted by the aqueous phase and the hydrocarbon tail are attracted by the oil phase. Co-surfactant is also used to stabilize the system. The nano-droplets can be used as micro-reactors carrying out chemical reactions. When the micelles contact with each other, the content inside the micelles will be mixed and the reaction can begin. In order to limit the reaction happens inside the nano-reactors, separate reverse emulsion should be prepared and then mixed.

In the past decades, RME method has been applied to many areas in order to synthesis shape and size controlled nanoparticles. Yang et al., [27] proposed core-shell structure silica coated aqueous quantum dots synthesized by reverse microemulsion method and the particle sizes can be controlled in a range of 45-109 nm. Vancher et al., [28] reported that the Prussian Blue

nanoparticles that prepared via RME method have uniform particle size and shape. The reaction inside the nano-droplet can limit the amount of reactant and leads to adjustable products.

Catalysts that prepared by RME method also showed superior performance and advantages compared with conventional methods. Kishida et al., [29] proposed that the Rh, Pd and Pt catalysts synthesized by RME methods showed much better performance for CO_2 hydrogenation than conventional wet impregnation method in terms of activity and selectivity towards methane. The improvement was considered to be the results of the decrease of the particle size. Zarur and Ying [30] deposit 25 wt% ceria onto BHA nanoparticles via RME method and the resulting catalysts have superior catalytic performance than BHA nanoparticles (**Fig. 8**). Furthermore, the ceria was able to remain the nano-crystalline morphology at 1300 °C while the bulk ceria would sinter and grow to more 100 nm at 700 °C.

Chapter 3 Methodology

3.1 X-ray powder diffraction

X-ray powder diffraction is a powerful method to identify the component and the crystal structure of the existing phase. Considering the wavelength of X-ray is close to the distance between atoms in the crystal (10-8 cm), German physicist M. von Laue proposed an important theory in 1912 that crystal can be seen as diffraction gratings for X-rays [31]. Diffraction occurs when a beam of X-rays passes through the crystal phases. Because of the superposition of the diffracted signal, the intensity of the signal is strengthened in some directions and weakened in others.

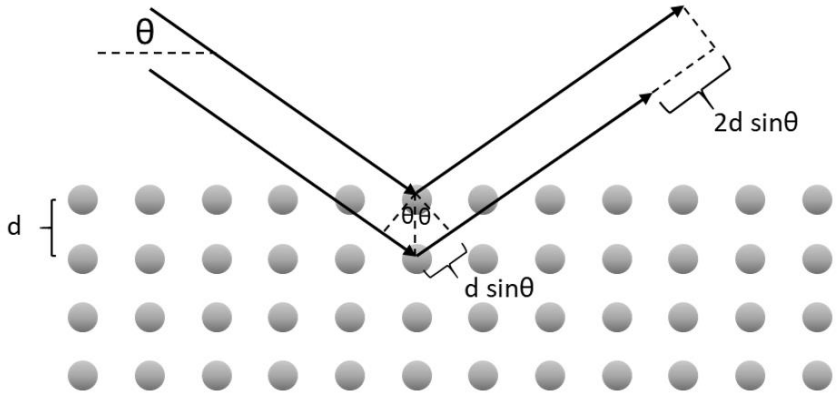

Fig. 9 Bragg's law schematic.

In 1913, the British physicist Dr. Bragg [32] proposed an equation based on Laue's discovery, Brag's law: $2d \sin\theta = n\lambda$. Where λ is the wavelength of the X-ray, n is any positive integer, d is plane spacing and θ is the grazing angle. The crystal structure can be determined by analyzing the diffraction pattern obtained on the photographic film. Each crystal will have its own peak

positions and intensities. Comparing with the standard JCPDS card, the crystal can be identified [33].

3.2 ICP-EOS

An atom or ion can be in a discontinuous state of energy. When an atom or ion in the ground state absorbs a certain amount of external energy, its extranuclear electrons transition from an energy state to a higher energy level. However, the atoms or ions in the excited state are very unstable and will transit to the ground state and radiate the absorbed energy with a certain electromagnetic wave. The wavelength of the electromagnetic waves generated from excited atoms is different. Since atoms or ions have many energy levels, particular atoms or ions can produce a series of characteristic spectra of different wavelengths, which will give the element information. The intensity of the wave at different wavelengths can be used to quantitatively analyze the content or concentration of an element in the sample after comparison with the standard curve.

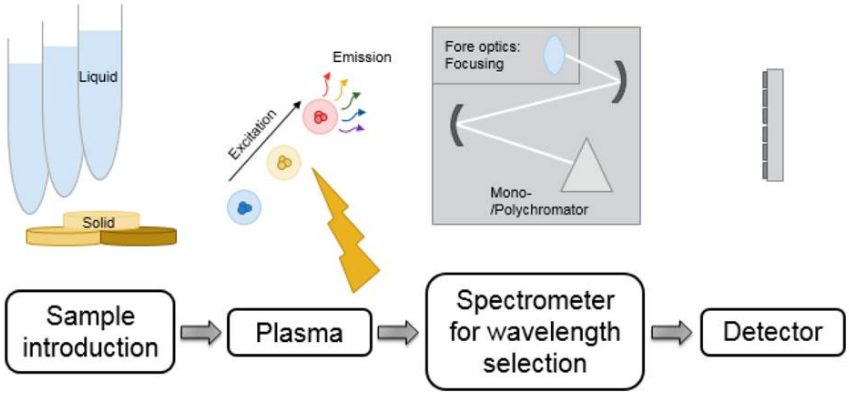

Fig. 10 ICP-OES schematic diagram.

3.3 Temperature-programmed reduction (TPR)

Temperature programmed reduction (TPR) method is one of the temperature-programmed analysis methods. In TPR experiment, a certain amount of metal catalyst is placed in a fixed bed reactor, and a reducing gas stream (usually a low concentration hydrogen) is passed through the catalyst at a specific flow rate while heating the reactor with a particular ramping rate. When the temperature inside the reactor reaches a specific value, the oxide on the catalysts begins to be reduced. Because the flow rate of the reducing gas is constant, the change in H_2 concentration after passing through the catalyst bed is proportional to the reduction amount of the catalyst.

The change of H_2 concentration is continuously detected by a gas thermal conductivity detector (TCD detector), and the curve was recorded to obtain a TPR curve of the catalyst. Each peak in the curve generally represents a reducible species or state in the catalyst, and the area integrated is proportional to the amount of consumed hydrogen. Information on the change of metal oxidation states, the interaction between two metals and the interaction between metal oxide and support can be deduced by TPR results.

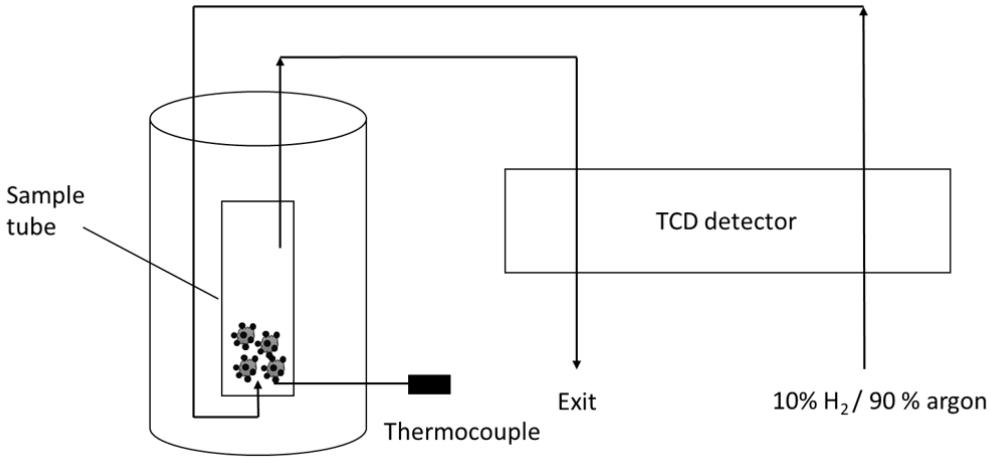

Fig. 11 TPR schematic diagram.

3.4 Surface area analysis (SAA)

Surface area analysis is based on the BET (Brunauer–Emmett–Teller) theory [34] which describe the adsorption of gas molecules on the solid surface. The specific surface area and pore distribution of the powder sample are usually evaluated according to the amount of adsorbed gas usually by a TCD detector. At a constant temperature, equilibrium state, a certain gas pressure corresponds to a certain amount of gas adsorbed on the solid surface and changing the pressure will affect the adsorption amount. When the sample is immersed in liquid nitrogen, gas nitrogen molecules that are passing through the sample will be physically adsorbed on the catalysts surface (chemical adsorption is avoided at low temperature). When the liquid nitrogen is removed, temperature raise up and nitrogen will desorb, and a negative peak will occur. The amount of adsorbed and desorbed molecules can be calculated by the area of the peaks.

BET model can be described by **eq. (8)**, where p is the pressure at equilibrium, p_0 is the saturated vapor pressure of the adsorbed gas at this temperature, V_m is the volume of gas required to form a monolayer on the surface, V is the amount of adsorption when the pressure is p, C is a constant.

After a series of p and V is obtained, $p/V(p_0-p)$ is plotted against p/p_0 plot, a straight line can be obtained. The slope of the line is $(C-1) / CV_m$ and the intercept is $1 / CV_m$ so that V_m and constant C can be deduced. Using the surface area equation, **eq. (9)**, the specific surface area can be obtained. Where NA is the Avogadro constant, s is the adsorption cross-sectional area of the adsorbed species, V is the molar volume of the adsorbed species and a is the quality of the adsorbent material.

$$\frac{P}{V(p_0-p)} = \frac{1}{V_m C} + \frac{C-1}{V_m C} \times \frac{p}{p_0} \tag{8}$$

$$S_{BET} = \frac{(V_m N_A s)}{V} \quad (9)$$

3.5 Scanning Electron Microscope (SEM) and Scanning Electron Microscope – Energy dispersive X-ray spectroscope (SEM-EDS)

Scanning Electron Microscope (SEM) is an electron microscope developed after transmission electron microscopy. A focused electron beam is generated from the source and this beam scans the surface of the sample point-by-point. After interacting with the sample, various physical signals are produced, amplified and converted into modulated signals by the detector, and finally displayed on the screen to present various features of the sample. SEM is strong in generating stereoscopic images, has large magnification range, allow continuous adjustment, has high resolution and is simple to prepare the sample.

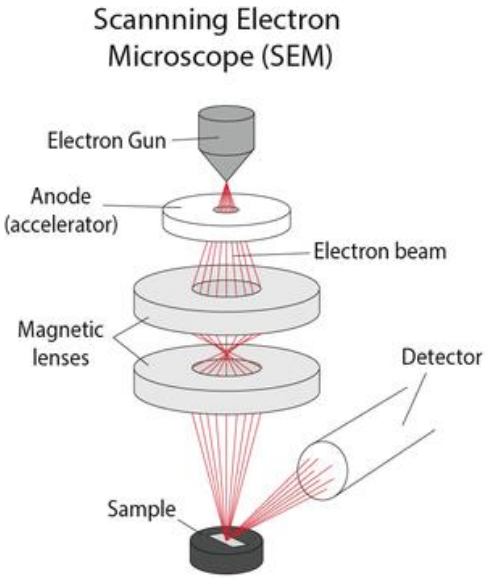

Fig. 13 SEM Schematic [1].

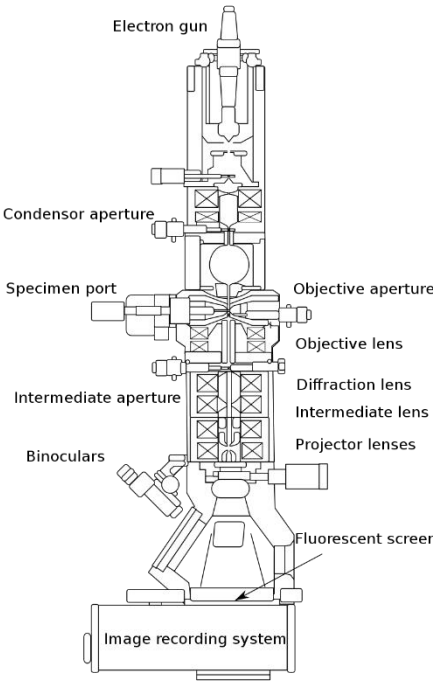

Fig. 13 TEM Schematic [2].

The combination of SEM and energy-dispersive X-ray spectroscopy (EDS) is often used to analyze the dispersion of the elements on the sample surface and EDS will provide the element

distribution and create a mapping for each element. This combination allows the researchers to connect the SEM spectrum and the dispersion of the elements.

3.6 Transmission electron microscopy (TEM)

Transmission electron microscopy is a high-resolution electro-optical instrument that the transmitted focused electrons transmit the sample to generate an image using an extremely short wavelength electron beam as the source. The most advanced TEM has a resolution of 1 nm and can directly observe atomic images. Since the spectrum is generated by transmission, the thickness of the sample should be ultrathin that the signal can go through and there should be only one layer of the sample. The TEM consists of an electro-optical system, a power supply and control system, and a vacuum system. When the electron beam passes through the sample, the transmitted electrons have different appearance information, showing different strengths. After the signal is processed and magnified, it is focused on a photographic screen that will provide the information of the sample.

3.7 Thermogravimetric Analysis (TGA)

Thermogravimetric Analysis (TG or TGA) is a thermal analysis technique that measures the relationship between mass and temperature of the sample that is heated at a certain ramping rate, to study the thermal stability and composition of the material. By analyzing the thermogravimetric curve, the temperature composition of the weight change and its intermediates, thermal stability, thermal decomposition, and product formation can be deduced. The thermogravimetric method is favoured by its high quantitative ability to measure the mass change and rate of change of a substance accurately [35]. Processes that all have mass change can be recorded and analyzed by TGA, such as sublimation, vaporization, adsorption, desorption, but

thermal behaviors such as melting and crystallization, do not involve mass change of the sample, which can not be analyzed by TGA method.

In this study, the reaction gas used in TGA is air and the experiments are temperature-programmed oxidation. The system was heated up slowly, and the weight change along with the temperature is recorded. The weight decrease in this study mainly represents desorption of the water or CO_2 on the surface and the oxidation of the deposition carbon during the reaction. The coking degree of our catalysts after reaction can be analyzed.

3.8 FTIR

3.8.1 In-situ FTIR

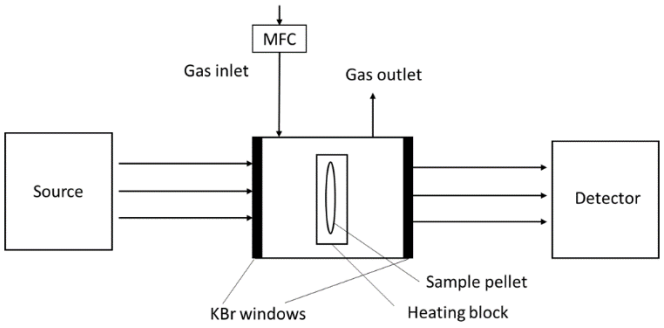

Fig. 14 in-situ FTIR schematic diagram.

Infrared spectroscopy belongs to the absorption spectrum and is based on the theory that the absorption of specific wavelengths of infrared is due to the compound molecules vibrate. [36] The wavelength of the infrared light absorbed depends on the chemical bond and the atomic weight of the atoms connected at both ends. This is the theoretical basis for the determination of the structure of compounds by infrared spectroscopy. Infrared spectroscopy is widely used as a "molecular fingerprint" for the study of molecular structure and chemical composition.

According to the relationship between the position, intensity, shape and absorption band of the peaks obtained by the absorption of infrared, it can be inferred that there is a certain group or bond in the molecule. In this study, the FTIR instrument used is a transition type. Inferred signal generated from the source goes through the sample pellet and the KBr windows at both sides of the pellet and arrives the detector (**Fig. 14**). Spectra are obtained at different temperature and at different reaction times to study the adsorbed species during the reaction.

3.8.2 IR detector for catalytic performance evaluation

The outlet stream of the reactor is measured continuously by an IR analyzer (IR-208 Infrared Industries). Target gases were analysed using a multiple channel infrared detector array. A single beam infrared goes through specially designed narrow band-pass optical filters and the energy of the inferred is limited to obtain the specified signal. The adsorption was compared with a specialized optical filter comparator and the concentrations can be accessed. The adsorption of CO_2, CH_4 and CO in the stream were measured at the same time and processed to digital signal for display.

Chapter 4 Experiment Setup

4.1 Catalysts synthesis

4.1.1 CoO_x/Al_2O_3 and CoC_x/Al_2O_3 by reverse microemulsion method

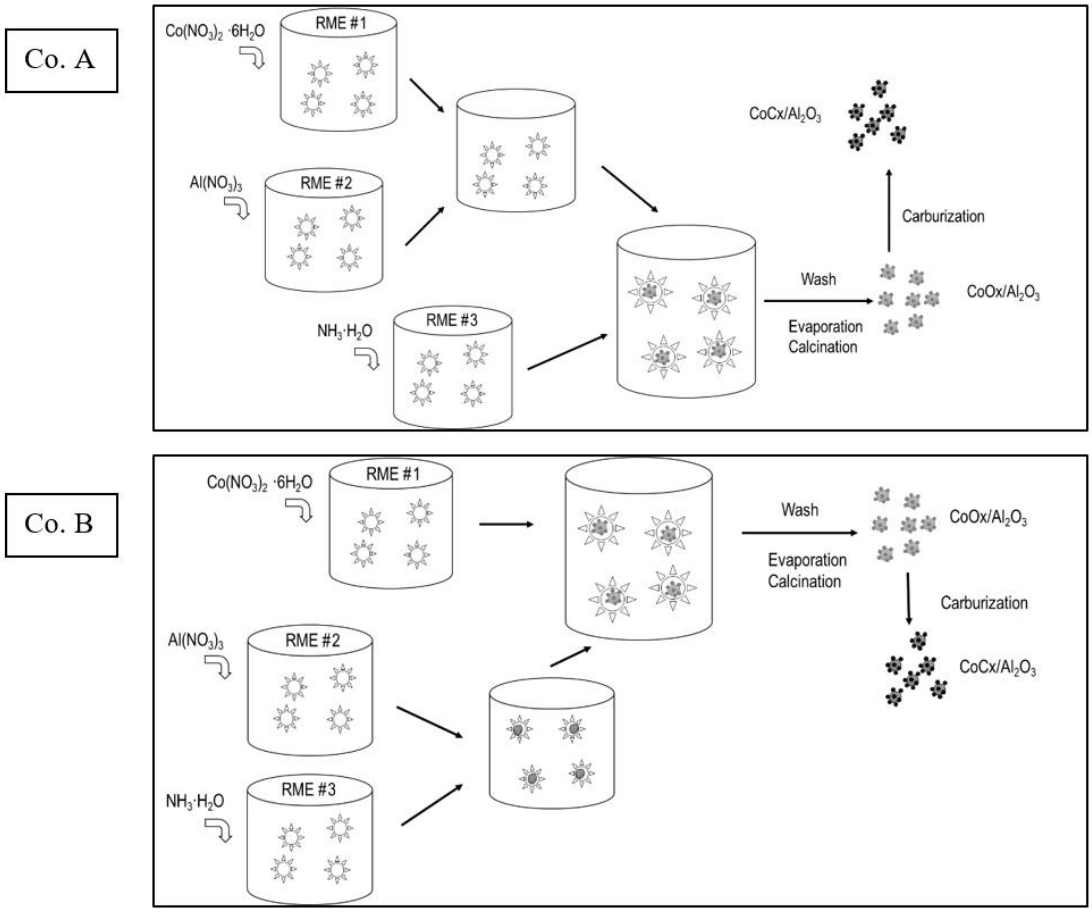

Fig. 15 Cobalt catalysts preparation procedure by RME method.

First, three blank RME's were prepared while mixing surfactant (Triton X-100, Acros Organics), Co-surfactant (propanol-2, Sigma-Aldrich) and oil phase in a ratio of 2:8:7 respectively under vigorous stirring. After, these blank RME's were used to prepare three individual RME's containing salt (Aqueous phase), i.e. cobalt nitrate hexahydrate, aluminium nitrate nonahydrate and ammonia and named as RME # 1, RME #2, and RME # 3 respectively. RMEs were prepared while adding aqueous phase to blank RME solution in the ratio of 3:2:8:7 (aqueous : surfactant :

co-surfactant : oil). Aqueous phases were prepared by dissolving cobalt nitrate hexahydrate (RME#1) and aluminium nitrate nonahydrate (Acros Organics) (RME #2) in deionized water to obtain 1 mol/L solution. 1 mol/L ammonia (LabChemq Inc.) was used directly for RME #3. After 15 min of stirring, aqueous phases were introduced to the blank RME's dropwise. After the addition of aqueous phases, a small amount of co-surfactant was added into the RME till the RME turned to transparent again.

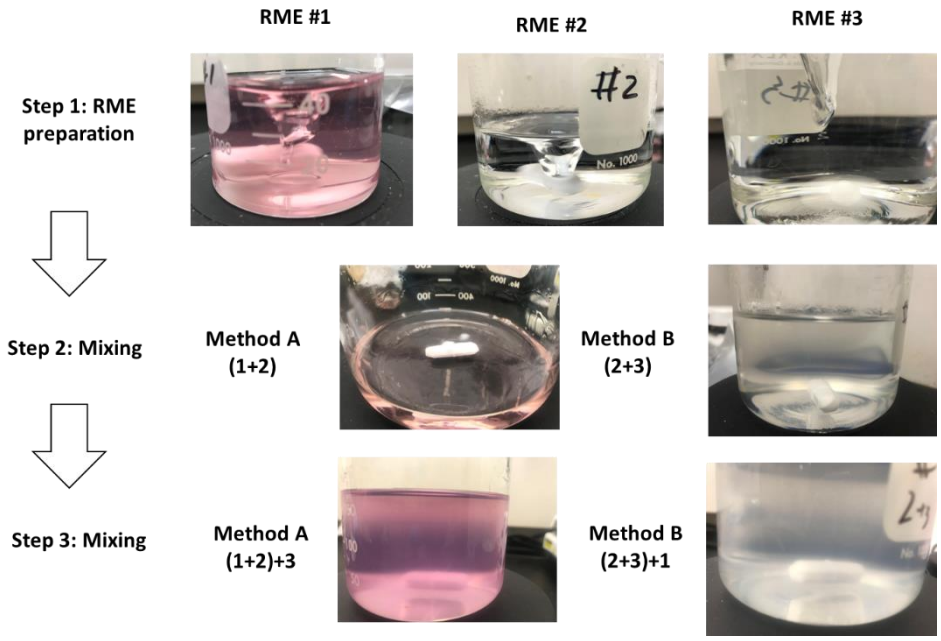

Fig. 16 RME preparation procedure.

Separately prepared cobalt nitrate, aluminum nitrate and ammonia RME's were mixed in different orders as described in **Fig. 15** and the changes of color and transparency are summarized in **Fig. 16**. Catalysts denoted as Co. A (CoO_x-A and CoC_x-A) were prepared by mixing RME #1 and RME #2 first under vigorous stirring of 1 hour and then RME #3 was introduced. The mixture of RME #1 and RME #2 was pink and transparent. When the mixture was added to RME #3, the RME system start to turn translucent because of the formation of alumina, β-$Co(OH)_2$ [37] [38]and also Co-Al double hydroxide [39]. The pink color of the RME is mainly due to the cobalt hydroxide

and the double hydroxide. After 8 hours under vigorous stirring, the mixture was stood overnight for stratification.

Catalysts denoted as Co. B (CoO_x-B and CoC_x-B) were prepared by mixing RME #2 and #3 for 8 hours first under vigorous stirring and then RME #1 was introduced. The mixture of RME #2 and RME #3 after 8 hours was translucent with a white undertone which due to the formation of alumina. After the addition of RME #1, the emulsion turned beige. The possible reason for the differences in the color between Co.A and Co.B is the pH in system B decreased after 8h of reaction and the form of cobalt hydroxide is mainly α-$Co(OH)_2$ since the required pH of α-$Co(OH)_2$ is lower than β-$Co(OH)_2$ [40]. Another possible reason is that the coordination compound $[Co(NH_3)_6]^{2+}$ (yellow) was formed and further oxidized to $[Co(NH_3)_6]^{3+}$ (brown) in the air.

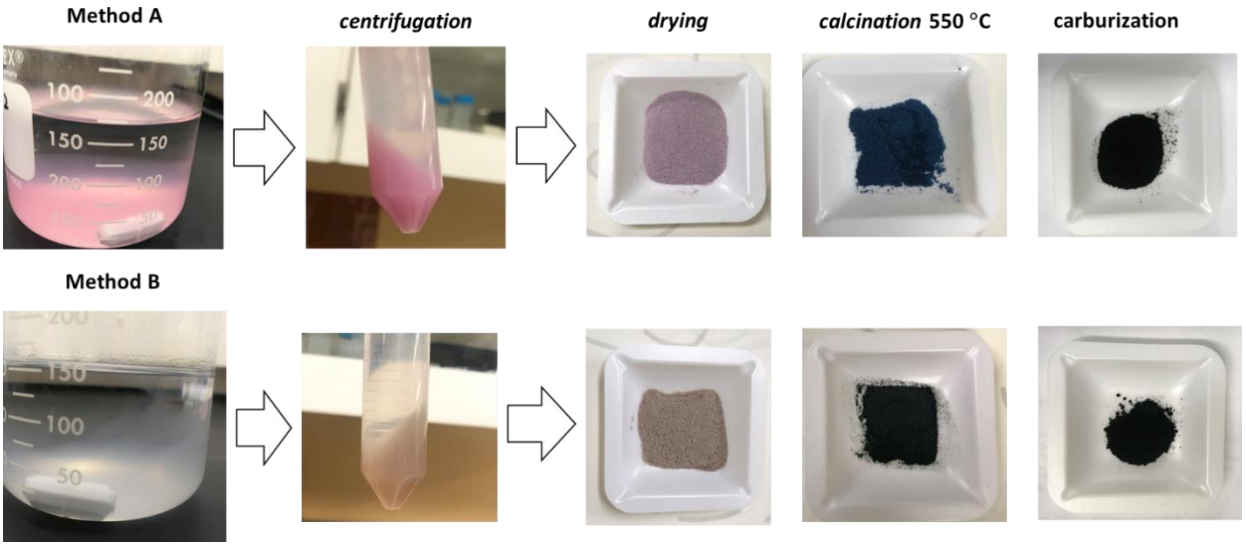

Fig. 17 CoOx and CoCx preparation procedure.

The precipitates were washed 3 times by ethanol and deionized water (3:1) followed by centrifugation. The resulted precipitates were dried at 100 °C, crushed to fine powder and

calcinated at 550 °C for 4 hours. This gives us cobalt oxides. CoO_x-A was navy as shown in **Fig. 17**, which indicated the existence of cobalt blue ($CoAl_2O_4$), a blue pigment[39], and the CoOx-B is a dark green powder which was a mixture of CoO and Co_3O_4 according to the XRD pattern (described in Chapter 5). To synthesis cobalt carbide, the oxides were carburized in the mixture of CH_4 (100 mL/min) and H_2 (400 mL/min) in a quartz tube from 250 °C to 800 °C with a ramping rate of 2 °C/min. The outlet stream from the carburization process was analyzed by an in-line FTIR analyzer (MultiGas^{TM} 2030, MKS Instruments). After carburization, both oxides turned into black powder.

4.1.2 Reference catalysts

12 wt% Co loading reference catalysts were prepared by wet impregnation method. Commercial alumina support was first crushed into fine powder and an appropriate amount of cobalt nitrate solution was added. After 2 hours of mixing, the suspension was dried at 100 °C and calcined at 550 °C same as the baseline samples. To obtain cobalt carbide, the results oxides was carburized at the same condition as RME catalysts.

4.2 Catalysts characterization

X-ray diffraction (XRD) patterns of the fresh and spent catalysts were obtained on a powder diffractometer (D8 Discover, Bruker). Temperature programmed reduction (H_2-TPR) of fresh and spent catalysts were carried out under pure hydrogen from 100 °C to 800 °C, with a ramping rate of 10 °C /min with the help of a catalyst characterization instrument (AMI-300Lite). Surface area analysis (SAA) was performed on the same instrument with single-point BET method. The degree of coking of the spent catalysts was investigated by thermal gravimetric analysis (TGA) attached in-Line with an FTIR analyser (MultiGas^{TM} 2030, MKS Instruments) conducted (referred

to In-situ TGA-FTIR). Scanning electron microscope (SEM), scanning electron microscopy coupled to energy dispersive spectroscopy (SEM-EDS) and Transmission electron microscopy (TEM) micrographs were obtained by a Zeiss microscopy to determine the shape and particle size distribution of as-prepared catalysts.

4.3 Flow system setup

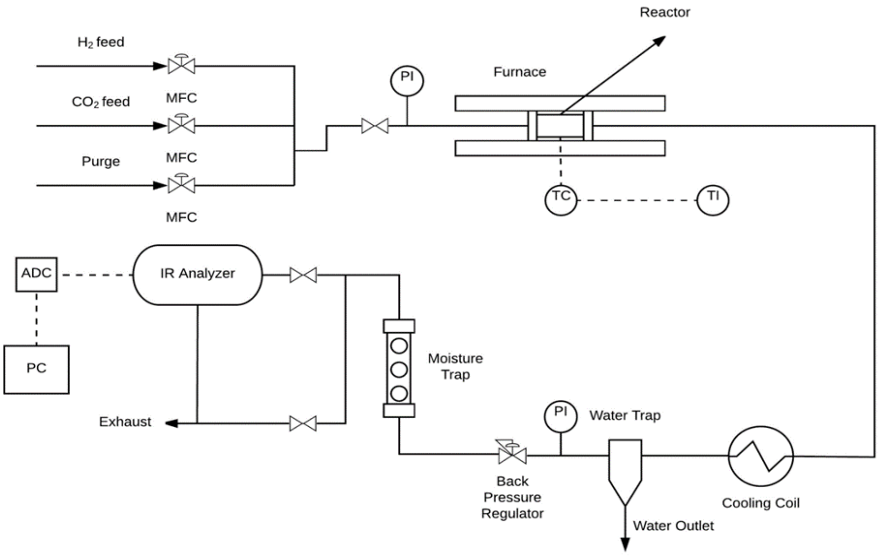

Fig. 18 Flow system setup.

A stainless-steel reducer (1/4" to 3/8") was used as the reactor, which was coupled between a 1/4" stainless steel tube at the outlet and a 3/8"tube at the inlet. 3/8" tube was used for the easy loading and unloading of the catalysts. Catalysts were loaded and sandwiched between quartz wool on both sides. After catalysts were loaded, the reactor system was placed in a programmable furnace (Lindberg/Blue M^{TM} Mini-Mite^{TM}, thermo Fisher Scientific). A K type thermocouple (1/8″, Omega Engineering) was installed at the outlet of the reactor touching the quartz wool next to the catalyst bed and connected to the controller (UP150, Yokogawa) of the furnace (Lindberg/Blue M^{TM} Mini-Mite^{TM}, thermo Fisher Scientific) for precise temperature measurement.

The pressure of the system was adjusted by a back-pressure regulator (S01094789B, Swagelok) while moisture was removed by a mist trap (AFM40-N02-Z-A, SMC Corporation) before the regulator and a silica gel (Fisher Scientific) column after as shown in **Fig. 18**. The composition of the dry outlet stream was measured by an IR analyzer (IR-208, Infrared Industries) continuously and monitored by an analog-to-digital converter (USB 6008, National Instruments) and LabView (National Instruments).

4.4 Catalytic performance evaluation

CO_2 methanation was investigated at different temperatures and pressures ranged 600-20 °C and 3-11 bar respectively. The CO_2 and H_2 inlet feed were controlled by two mass flow controllers and maintained at H_2:CO_2=4:1. Before introducing CO_2, the catalysts were reduced under pure H_2 (300 mL/min) environment at 350 °C for 2 h. For each point, the temperature or pressure was kept for 2h until the concentration is stable.

Gas hourly space velocity (GHSV) was maintained at 60,000 mL g_{cat}^{-1} h^{-1} for all catalytic performance tests and was calculated using the following equation:

$$GHSV = Q_f / W_C \tag{10}$$

In **eq. (10)**, Q_f and W_C are the volumetric flow rate and the weight of the catalysts respectively. CO_2 conversion and CH_4 selectivity were determined by **eq. (11)** and **eq. (12)**. y_{CO_2} , y_{CH_4} and y_{CO} represents the mole fraction of CO_2, CH_4, and CO respectively on dry basis. X is the conversion and S is the selectivity.

$$X_{CO_2} = \frac{y_{CO}+y_{CH_4}}{y_{CO_2}+y_{CO}+y_{CH_4}} \tag{11}$$

$$S_{CH_4} = \frac{y_{CH_4}}{y_{CO}+y_{CH_4}} \quad (12)$$

Carbon balance of the system is given by **eq. (13)**. Where, α is the ratio of H_2/CO_2 in the feed, f_1 and f_2 are the conversion to CO and CH_4 respectively, $F_{C,out}$ is the outlet molar flow rate [41].

$$CB = (y_{CO_2} + y_{CO} + y_{CH_4})(1+\alpha - f_1 - 4f_2) \quad (13)$$

$$\alpha = \frac{F_{H_{2,f}}}{F_{CO_{2,f}}} \quad (14)$$

$$f_1 = \frac{y_{CO}}{y_{CO_2} + y_{CO} + y_{CH_4}} \equiv \frac{F_{CO,out}}{F_{C,out}} = \frac{F_{CO,out}}{F_{CO_2,f}} \quad (15)$$

$$f_2 = \frac{y_{CH_4}}{y_{CO_2} + y_{CO} + y_{CH_4}} \equiv \frac{F_{CH_4,out}}{F_{C,out}} = \frac{F_{CH_4,out}}{F_{CO_2,f}} \quad (16)$$

3.5 In-situ FTIR study

To investigate the reaction mechanism over the catalysts surface, in-situ FTIR spectra were obtained using an IR cell placed in an FTIR spectrometer (Thermo Scientific™ Nicolet™ iS™5) and attached with the catalyst characterization instrument (AMI-300Lite). Inlet and outlet flow were connected to the instrument and went through the cell. A bed thermocouple connected with a controller was employed to control the temperature. For each spectrum, each catalyst was pressed to a KBr pellet support and reduced in H_2 (10% H_2/Ar) at 350 °C for 1 hour followed by argon flushing before introducing reaction gases (2% CO_2/8% H_2/90% Ar, 30 mL/min). Background spectra were taken at the same temperature under argon (30 mL/min). The spectra were studied at

different temperature (100 °C, 200 °C, 300 °C and 400 °C) and time evolution of the spectra was accessed at 350 °C.

Chapter 5 Results and discussion

5.1 Characterization

Table 2: Characteristic of fresh catalysts

	Co loading (wt %)	BET surface area (m^2/g)	cobalt crystallite size (nm)
RME Al_2O_3	0	380	-
CoO_x-A	11.0	272	8
CoO_x-B	10.4	249	4
CoC_x-A	12.8	200	4
CoC_x-B	11.3	178	6

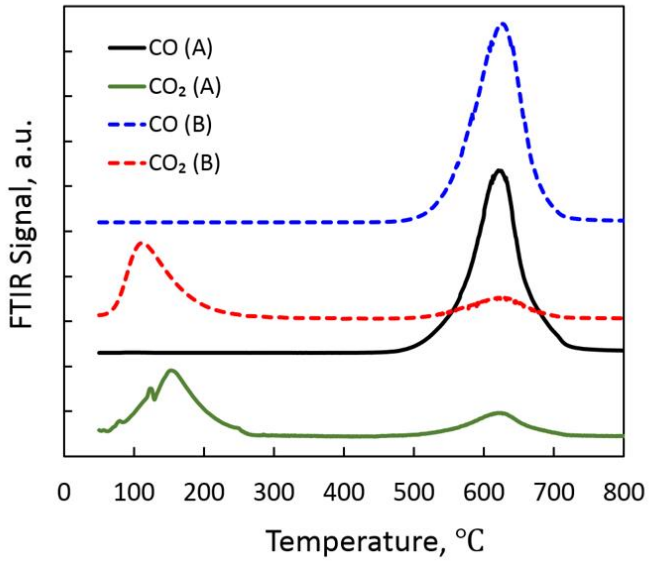

Fig. 19 CO and CO_2 profile during carburization process. Heating rate = 2 °C/min.

Fig. 19 shows the carburization process for Co. A and Co. B oxide. It can be easily seen that both catalysts undergo almost similar conversion process, as the peak locations were almost identical. The weak CO_2 peak appears below 200 °C may due to the desorption of adsorbed CO_2 from the catalysts surface. The large peak of CO and the other weak peak of CO_2 at 620 °C were

assigned to the reaction products from carburization. Most of the product of carburization is CO and the amount of CO recorded was 15 times higher than the CO_2 emitted during the process. It is the fact that, CO is easier to generate from CH_4 in kinetics when it is excess during the reaction.

Table 2 shows the catalysts composition determined by ICP-OES, BET-SSA (Specific surface area analysis) and particle sizes calculated by Scherrer equation using XRD data. The cobalt loading of each catalyst maintained consistency while the cobalt loading of RME carbides were a little higher than the number of oxides, as a result of the composition transfer during the carburization process. Carbon replaces the oxygen and the oxidation state of the cobalt also changed. Comparing with the alumina support synthesized by RME method, the surface area for supported oxides decreased approximately 26% and the number declined again for around 20% after carburization. The difference of the surface area number between alumina support and alumina-supported cobalt oxide was because of the existence of cobalt oxide that blocked part of the surface. [42] During carburization, the sintering of the catalysts at high temperature will further decrease the surface area.

Fig. 20 represents the XRD patterns for the fresh and spent catalysts (after temperature test). The possible reason for the board peaks is the size of the particle prepared from RME method was quite small as shown in Table 1 and all particles were well dispersed on the support [42]. Also, the loading of cobalt in all samples are relatively low, and the XRD patterns are dominated by the alumina. The nanosized particles usually lead to lower crystallinity and will widen the XRD peaks. Pure alumina support synthesized by RME method was also tested for comparison. The two peaks appeared at $2\theta=45°$ and $2\theta=66°$ were assigned to γ-Al_2O_3. With the joining of cobalt, additional peaks can be observed in CoO_x samples. These peaks were assigned to cobalt oxide species. [43]

After carburization process, the cobalt oxide peaks disappeared as expected and peaks for Co_2C (42.7° JCPDS card no. 050704), Co_3C (JCPDS card no. 260450) appeared.

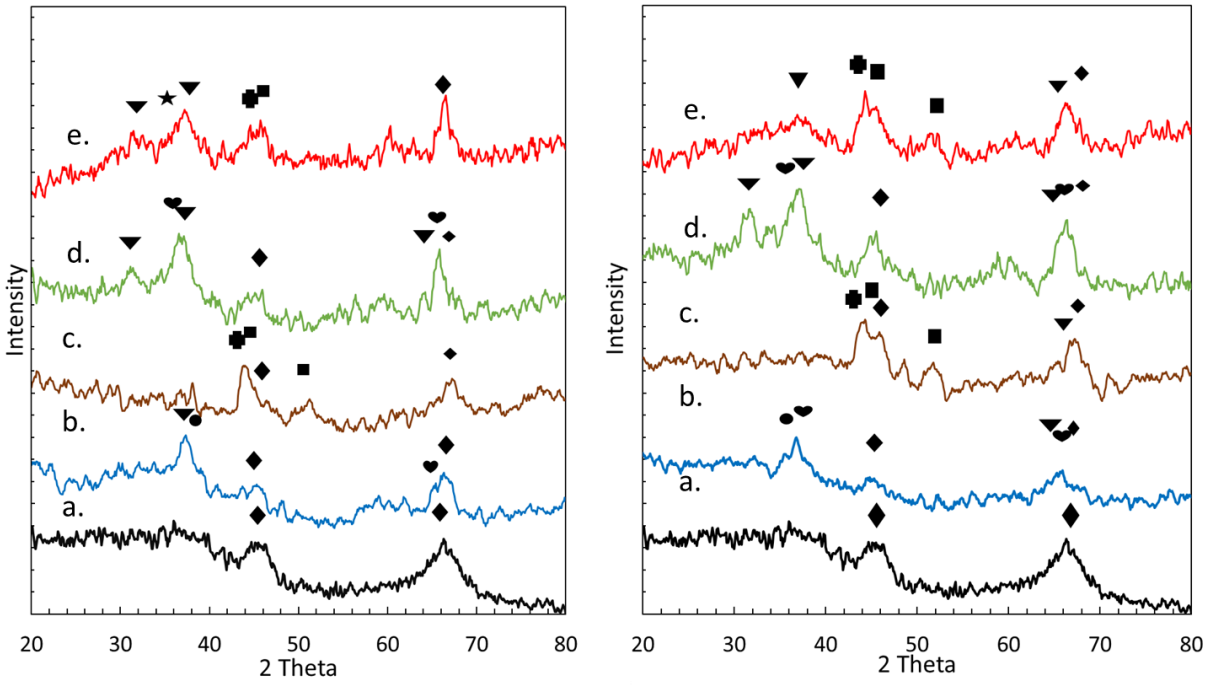

a. RME Al_2O_3 b. Fresh CoO_x-A c. Fresh CoC_x-A d. Spent CoO_x-A e. Spent CoC_x-A

a. RME Al_2O_3 b. Fresh CoO_x-B c. Fresh CoC_x-B d. Spent CoO_x-B e. Spent CoC_x-B

Fig. 18 XRD patterns of CoO_x and CoC_x. ♦: Al_2O_3; ●: CoO; ■: Co_3C; ⯃ :Co_2C; ▼: $CoAl_2O_4$; ♥: Co_3O_4; ★:carbon.

Interestingly, $CoAl_2O_4$ was also detected and was more evident in the samples that $Al(NO_3)_3$ RME and $Co(NO_3)_2$ RME were mixed first (Co.A). Studies reported that $CoAl_2O_4$ could be synthesized by cobalt and aluminum nitrate solution followed by calcination [39, 44]. However, even cobalt nitrate and aluminum nitrate were mixed first, the entering of ammonia will still react with most of the aluminum nitrate due to different reaction selectivity and preference. In **Fig. 20**, peaks for $CoAl_2O_4$ became evident after the reaction and the cobalt carbide peaks has been weakened. $CoAl_2O_4$ was more likely to form at higher temperature, so the reaction at 600 °C can be seen as another calcination. While Co_2C and Co_3C are easier to be reduced to cobalt metal phase

with a temperature under 400 °C and cobalt oxide will need higher temperature [45]. This viewpoint was also demonstrated in the TPR files (**Fig. 21**). The TCD signal of oxide samples continued going up to 800 °C and showed the incomplete reduction even at this high temperature.

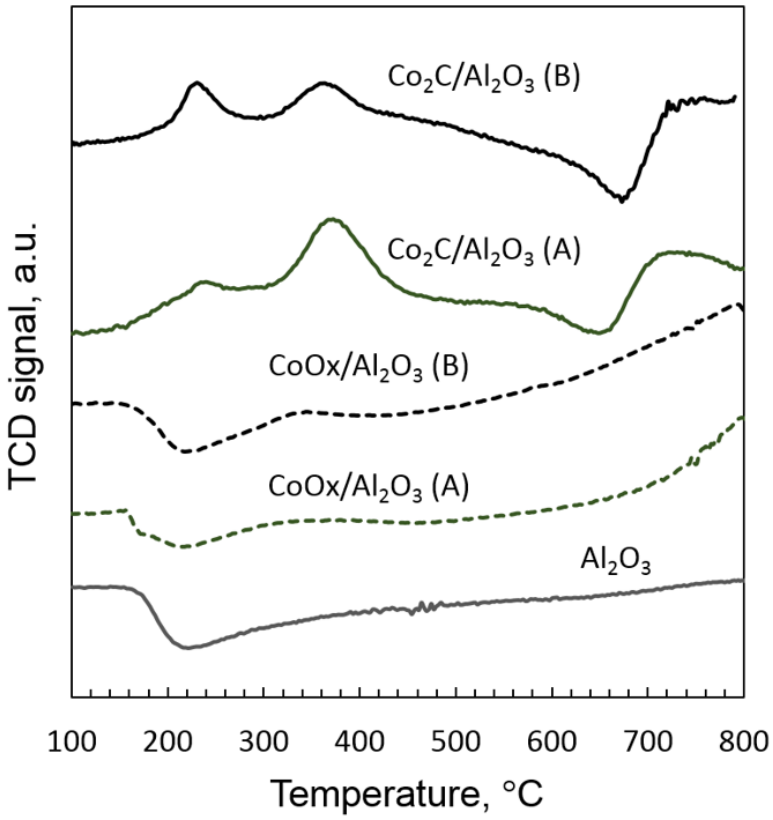

Fig. 21 TPR patterns of fresh CoOx and CoCx. Catalysts were pre-treated in argon at 150 °C for 30 min. Heating rate = 10 °C /min.

H_2-TPR was also performed to investigate the reducibility of the catalysts. The weak peak observed under 500 °C in CoO_x-A and CoO_x-B can be assigned to Co_3O_4 reduced to CoO [46] and the peaks start from 500 °C belongs to CoO further reduction to cobalt metal [47] [48]. The sustained growth of TCD signal until 800 °C indicated the relative composition of Co_3O_4 and CoO. After holding at 800 °C for 1 hour, the TCD signal went back to baseline showing the completion

of the reduction process. The consumption of H_2 can be calculated according to the peak area of the TCD signal and provide an approximate ratio of Co_3O_4 and CoO. It can be suggested that CoO content in the cobalt oxide phase was much higher than Co_3O_4. There are two major picks appeared in cobalt carbide catalysts that one is around 200 °C and the other is around 350°C. The peak positions in TPR pattern will give a potential optimal reaction temperature in methanation. Interestingly, during the catalytic performance evaluation, the temperature that gives the best activity is around 400 °C.

Fig. 22 shows the Scanning electron microscope graphs for all fresh catalysts and appeared having the same morphology. The particles have a porous surface, providing a high surface area in agreement with the BET results. SEM-EDS elemental mapping was also conducted to investigate the dispersion of the catalysts. As showed in **Fig. 23**, it is clear to see cobalt was well dispersed on the alumina support.

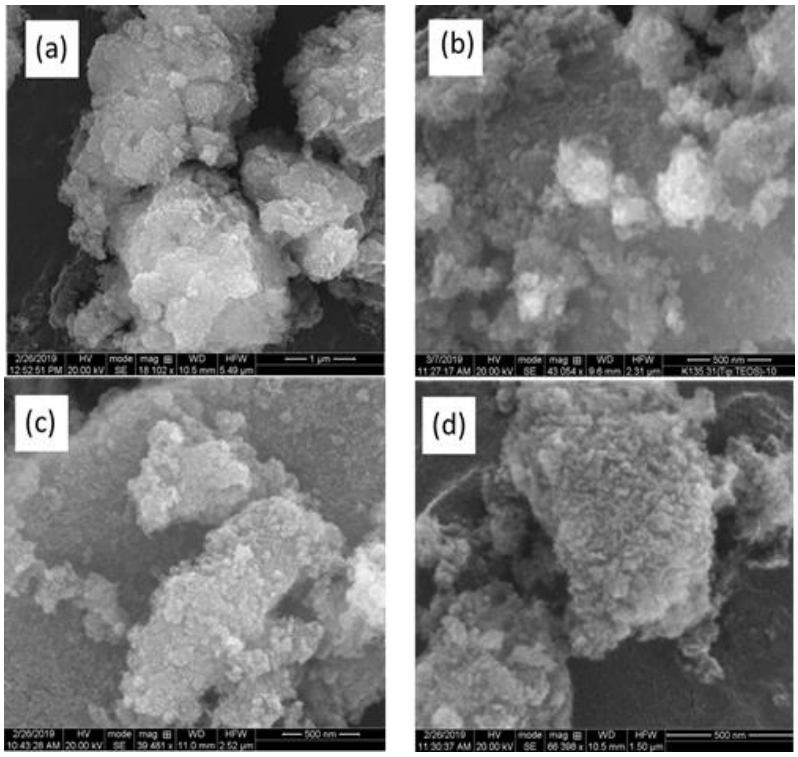

Fig. 22 SEM micrographs of fresh CoO_x and CoCx. (a) CoO_x-A; (b) CoO_x-B; (c) CoC_x-A; (d) CoC_x-B.

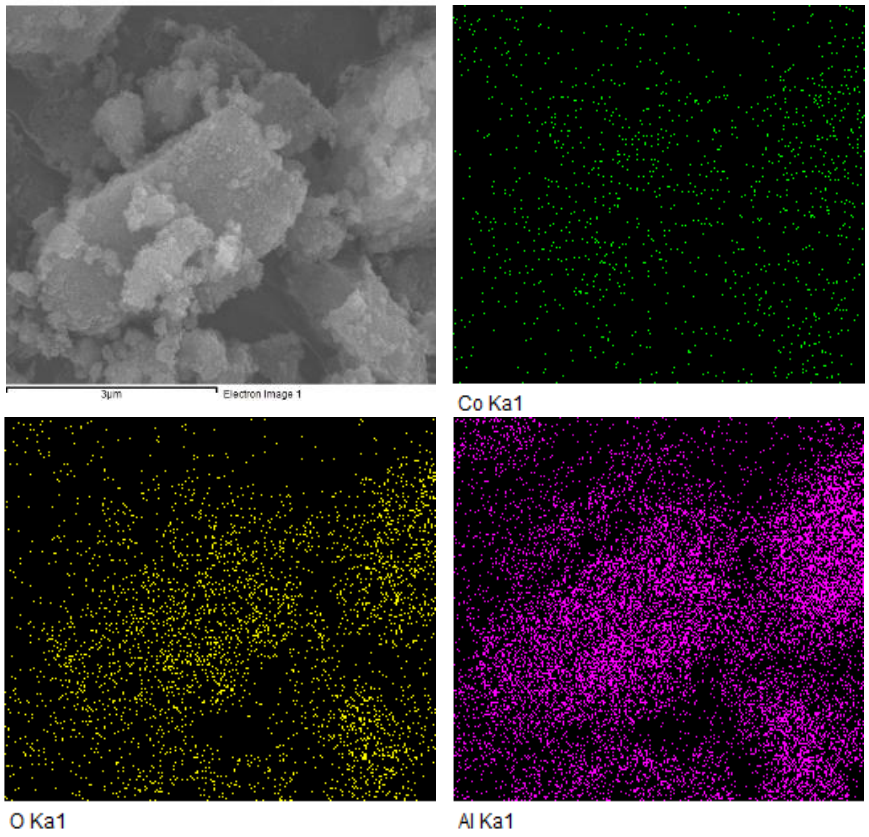

Fig. 23 SEM-EDS mapping of CoC_x-A.

TEM micrographs were obtained to further study the dispersion and existing form of particles. In **Fig. 24**, the alumina support can be seen clearly as nanorods crossing with each other with a 5 nm diameter, 20-40 nm length. Cobalt oxide and cobalt carbide particles exist in the form of rounded shape nanoparticles and all attached evenly to the nanorods [49].

TEM micrographs of the catalysts spent from temperature test were also obtained to investigate the morphology changes before and after the reaction. The lattice structure was even clearer after 12 hours reaction, which may be due to the calcination effect during the reaction.

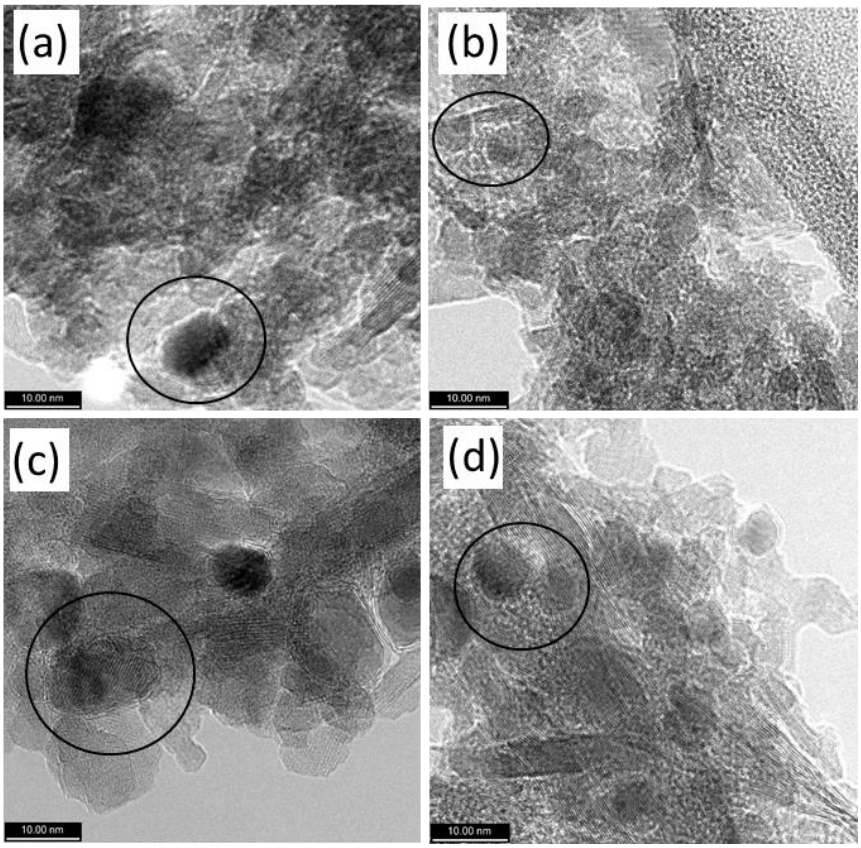

Fig. 24 TEM micrographs of supported catalysts: (a) fresh CoC_x-A; (b) fresh CoC_x-B; (c) spent CoC_x-A; (e) spent CoC_x-B.

5.2 Catalytic performance evaluation

The catalytic performance of the catalysts was investigated on CO_2 methanation in terms of varying temperature and pressure (absolute pressure) with GHSV=60,000 mL g_{cat}^{-1} h^{-1}. **Fig. 25** indicated the activity and selectivity of all the as-prepared catalysts and reference catalysts at different temperature. For both samples prepared by RME method and reference samples, cobalt carbides showed superior performance than cobalt oxides, especially at lower temperature. The activity of oxides all decreased rapidly from 500-300 °C and conversion of CO_2 were all below 20% at 300 °C. The rising tendency of the CO_2 conversion on two RME carbides continued as the

temperature went down to 400 °C and reached 0.78 and 0.77 respectively, and then a small decline appeared at 300 °C (0.74 and 0.71).

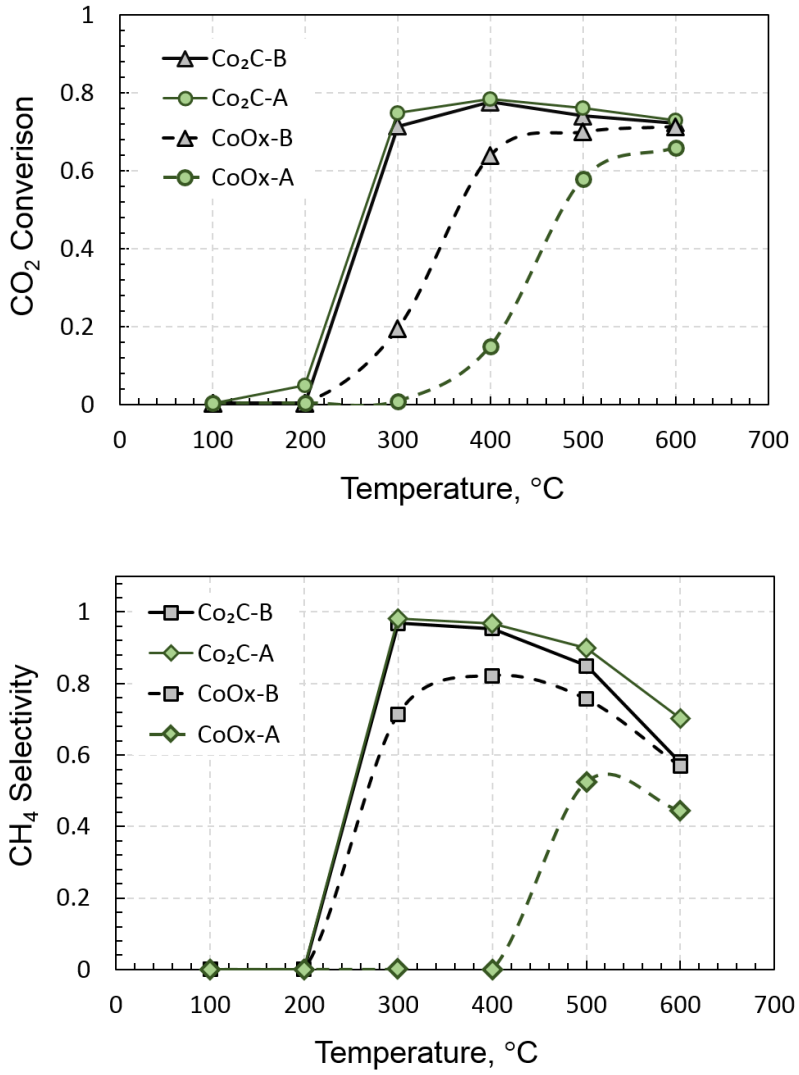

Fig. 25 Catalytic performance of CoO_x and CoC_x prepared by RME method at different temperature. All the catalysts were reduced in hydrogen at 350 °C for 2h before reaction. Reaction condition: CO_2:H_2 = 1:4, GHSV = 60,000 mL g_{cat}^{-1} h^{-1}.

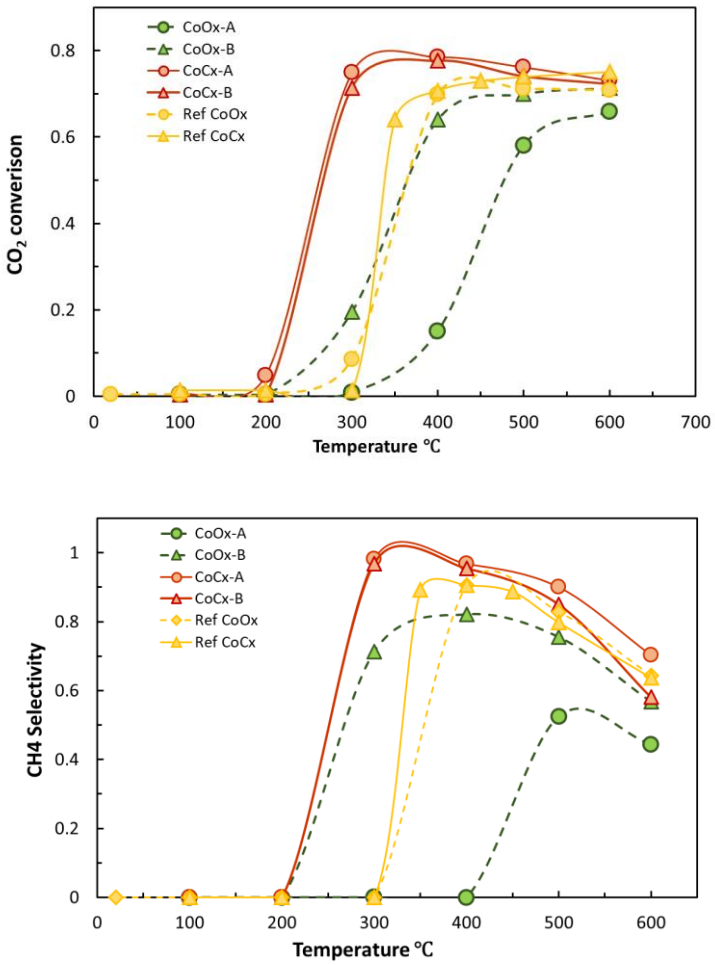

Fig. 26 Comparisons of catalysts prepared by RME and wet impregnation. All the catalysts were reduced in hydrogen at 350 °C for 2h before reaction. Reaction condition: CO_2:H_2 = 1:4, GHSV = 60,000 mL g_{cat}^{-1} h^{-1}.

Comparing with the reference cobalt carbide catalyst that was prepared from conventional wet impregnation method, CoC_x-A and CoC_x-B showed higher conversion of CO_2 and selectivity to CH_4. In **Fig. 26** the superiority was more significant in the reaction temperature region of 300-400 °C. As for selectivity, there was a general trend that the selectivity declined with the rising temperature, and the peak always showed at the temperature where the reaction started to occur. In particular, the selectivity of CoO_x-A and CoO_x-B sample can achieve over 0.96 with a conversion over 0.71 at 300 °C which is promising as a catalyst for CO_2 methanation.

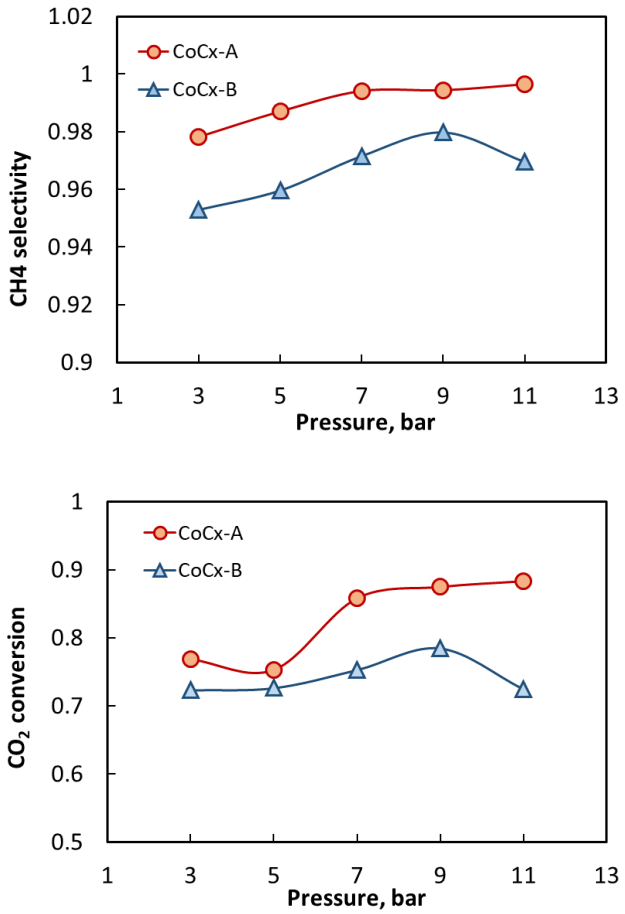

Fig. 27 Catalyst performance of CoC_x-B at different pressure. Catalysts was reduced in hydrogen at 350 °C for 2h before reaction. Reaction condition: Temperature = 350 °C, CO_2:H_2 = 1:4, GHSV = 60,000 mL g_{cat}^{-1} h^{-1}.

Conversion of CO_2 and selectivity towards CH_4 as a function of pressure on two RME carbides were shown in **Fig. 27**. According to Le Chatelier's principle, [50] the conversion of CO_2 increases with the pressure and the methanation reaction is also favored under higher pressure comparing with reverse water gas shift reaction. Though for CoC_x-B, activity decreased as the pressure went up from 9 bar to 11 bar, which may due to the degradation of the catalyst and requires further investigation, the overall performance was proportional to the total pressure. The conversion over CoC_x-A continued rising after a slight decrease at 5 bar and finally achieved 0.9 at 11 bar which provided a promising condition for industrializing production.

It can be concluded that CoC_x-A has the most superior performance among all the baseline and reference samples. CoC_x-B also showed identical activity over testing temperature range but lower selectivity at high temperature above 400 °C.

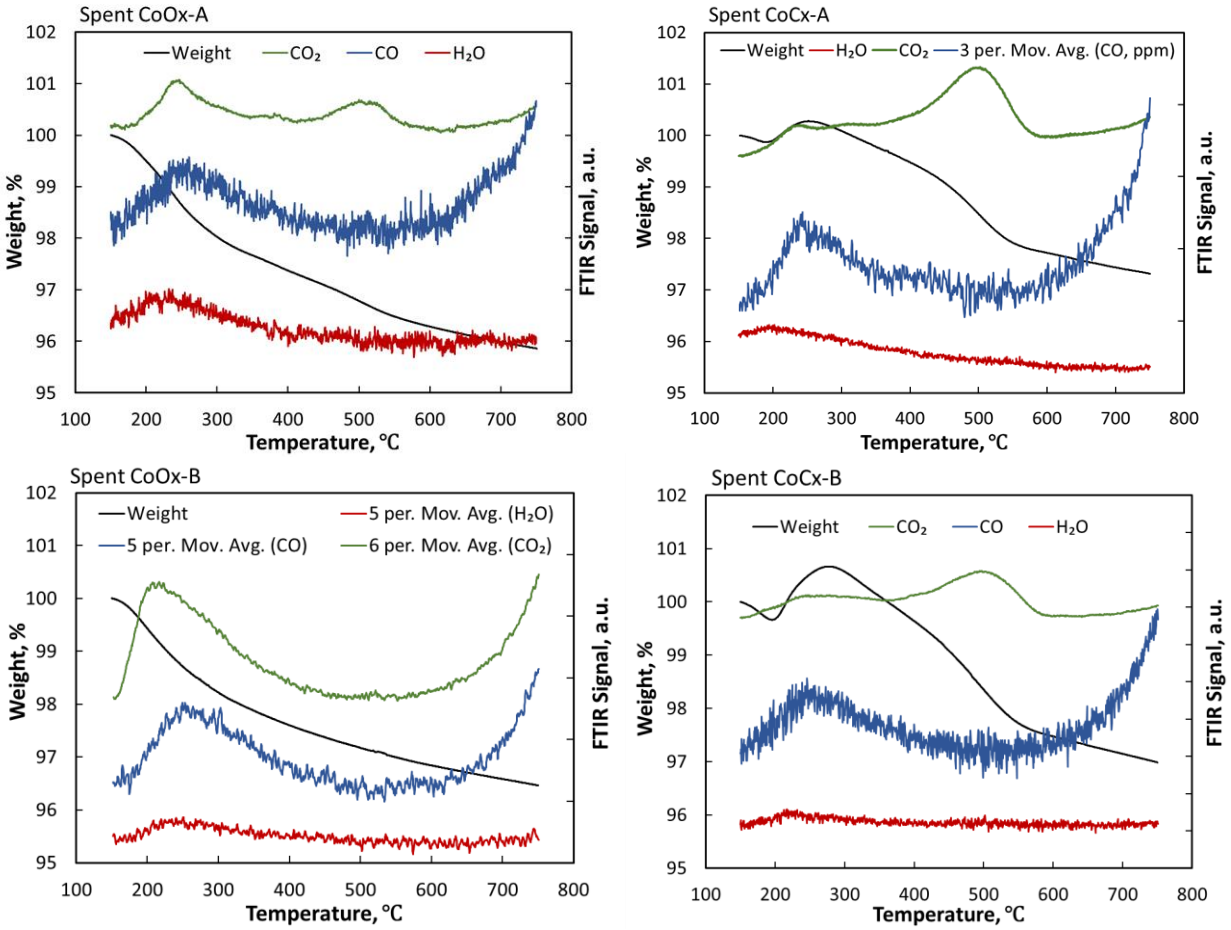

Fig. 28 TGA-FTIR analysis for spent catalysts.

TGA-FTIR study was conducted to understand the carbon deposition degree after temperature test as shown in **Fig. 28**. All RME samples lost around 4% of their total weight from 250 °C to 800 °C. The CoC_x-A and CoC_x-B sample gained approximately 1% weight from 200 °C to 300 °C which may demonstrate the oxidation of carbide species in the cobalt carbide phase, and

then a 4% weight loss occur which was the oxidation of the deposition carbon on the catalysts surface.

5.3 In-situ FTIR study

In-situ FTIR studies were conducted to investigate the adsorbed species on the cobalt oxide catalysts during CO_2 methanation. **Fig. 29** shows the spectra of cobalt oxide at different temperatures under the reaction gas. The adsorbed species on CoO_x-A and CoO_x-B showed identical positions. At 100 °C, adsorbed CO_2 species were observed. As the temperature went up to 400 °C, the peaks of adsorbed CO_2 decreased gradually, and the formate species occur along with the appearance of gas phase CO peak.

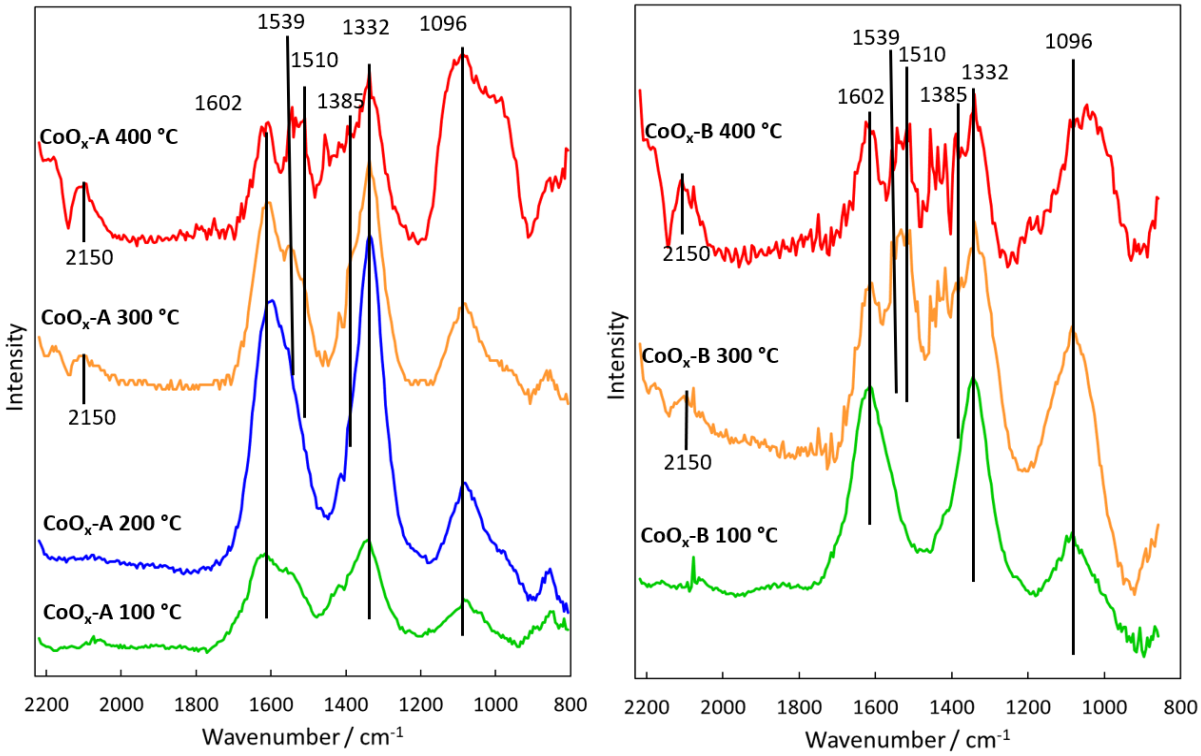

Fig. 29 In-situ FTIR spectra as a function of temperature of CoO_x samples, after 15min reaction under 2% CO_2 /8%H_2/Ar.

It can be deducted that CO is part of the methanation process. In **Fig. 29**, peaks at 1602 cm^{-1}, 1332 cm^{-1}, 1096 cm^{-1} were assigned to adsorbed CO_2 which consistently appeared at every temperature [51]. When the temperature went up to 300 °C, the peak of gas CO (2150 cm^{-1}) started to show up indicating the occurrence of the reaction [52]. Meanwhile, peaks of formate species were detected. The peaks at 1539 cm^{-1}, 1510 cm^{-1} represent the formate species adsorbed on the surface which suggested a pathway through formate of the reaction [53].

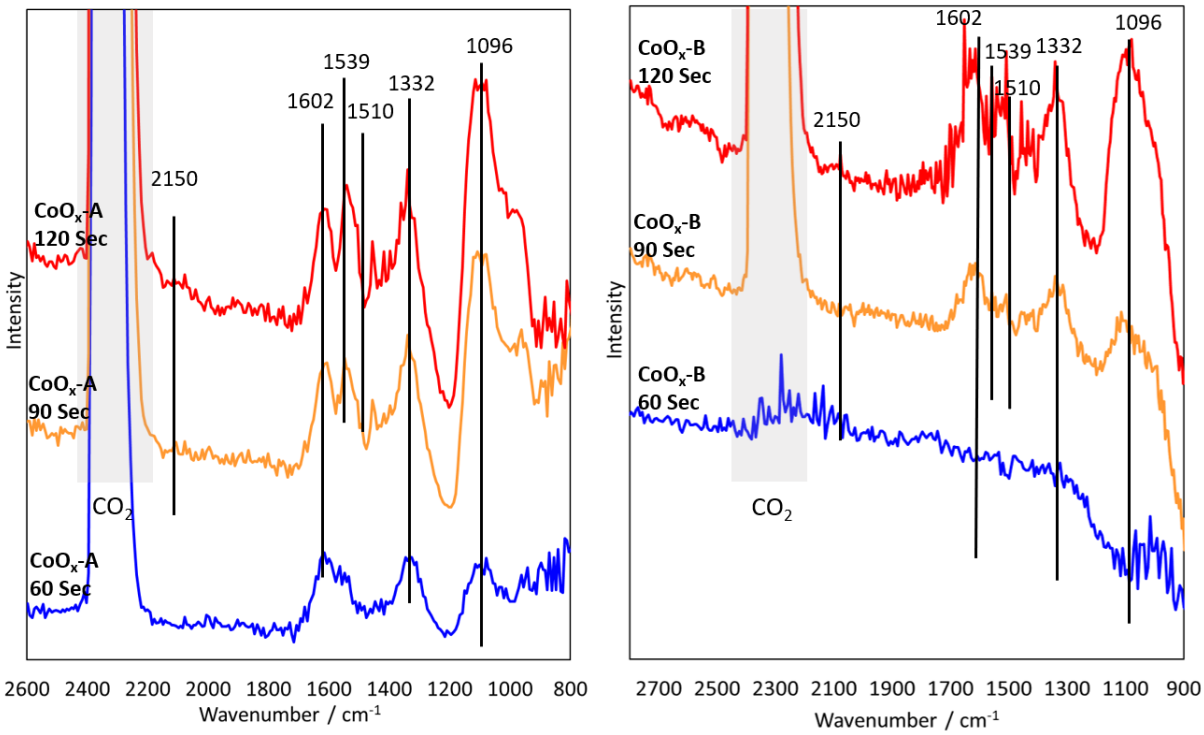

Fig. 30 In-situ FTIR spectra as a function of time of CoO_x samples, at 350 °C under 2% CO_2 /8%H_2/Ar.

The spectrum evolution with time was also investigated. **Fig. 30** illustrated the transformation of the spectrum after CO_2 and H_2 were introduced to the system. At the point only a little amount of CO_2 contacted the catalysts, the concentration of the reactant gas was not enough to activate the reaction and can only be adsorbed on the surface as physical adsorption. When more

CO_2 and H_2 entered the cell, a reaction concentration was reached, and the adsorbed species were reacted turning to intermediate species appeared on the surface.

In-situ FTIR is also addressed on the cobalt carbide catalysts. Due to the poor transmittance of the carbide samples, the ratio of signal to noise is lower than the oxide. Adsorbed CO_2 species in different forms dominate all the spectra. The peaks of adsorbed species were unable to identify for CoC_x-B at 300 °C. Same as oxides samples, phase CO is observed from 200 °C and peaks for formate species appeared. In **Fig. 31**, the peaks appeared at 1586 cm^{-1} was assigned to carboxylate and the peaks at 1406 cm^{-1}, 1337 cm^{-1} and 1070 cm^{-1} represent adsorbed carbonate species. The weak peak appears at 1391 cm^{-1} may due to formate. [54]

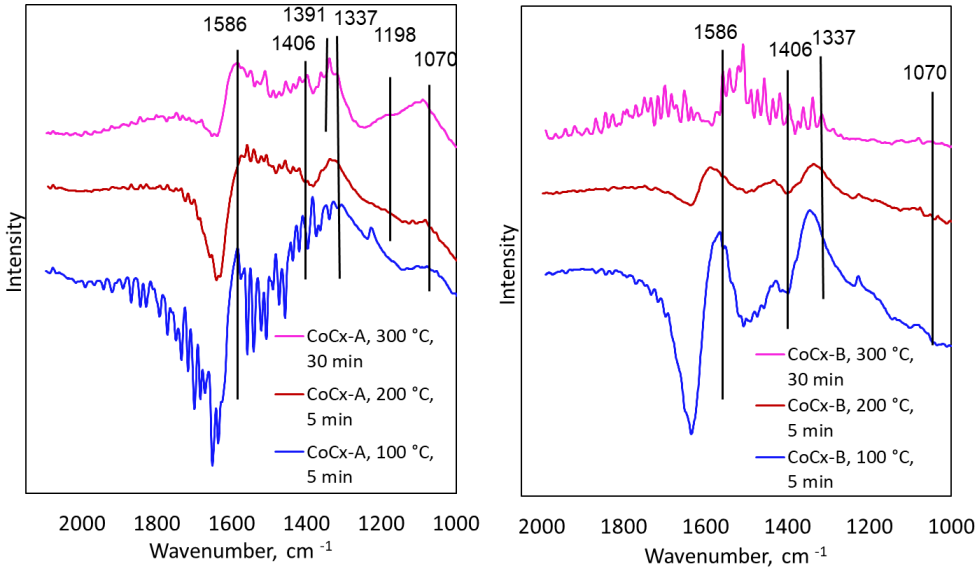

Fig. 31 In-situ FTIR spectra as a function of temperature of CoC_x samples, after 15min reaction under 2% CO_2 /8%H_2/Ar.

Chapter 6 Conclusion and future work

6.1 Conclusion

To obtain an active and economically viable thermo-catalyst for CO_2 methanation, highly active and selective alumina-supported cobalt carbide catalysts were successfully synthesized by the reverse microemulsion method. Investigations of the composition, crystalline phases and morphology of the catalysts were carried out by XRD, TPR, SEM and TEM. XRD study proved the existence of the cobalt carbide phase in the catalysts and SEM-EDS indicated excellent dispersibility. TEM showed the cobalt oxides and carbides are nano-sized particles from 5-15 nm attached on the alumina nanorods. TPR curves indicated the reducibility of the catalysts. The area of the peaks suggested that CoO is dominated in the cobalt oxides. Co_3O_4 was reduced to CoO before 500 °C and CoO was further reduced to metal cobalt after 500 °C. Two reduction peaks appeared in cobalt carbide catalysts which guided to two possible optimal methanation temperature (200 °C and 350 °C).

The catalytic performance was tested on CO_2 methanation and cobalt carbide catalysts showed superior advantages. At 400 °C, 3 bar pressure, the conversion of CO_2 on carbide catalysts were over 78% and the selectivity towards CH_4 were over 96%. When the pressure was increased, the conversion, as well as the selectivity, was further improved. The best performance was achieved on CoC_x-A, at 350 °C and 11 bar pressure, with a 91% conversion and 98% selectivity. This temperature is agreed to the TPR results that the highest conversion temperature appeared around the second peak.

In-situ FTIR study was conducted to investigate the mechanism of the methanation reaction on the supported cobalt oxide and cobalt carbide catalysts prepared by the reverse microemulsion

method. A pathway through formate of CO_2 hydrogenation via CO was suggested by the FTIR study. At lower temperatures and lower gas concentrations, CO_2 was physically adsorbed on the surface. When the reaction conditions were achieved, formate species, which are the intermediates adsorbed on the catalysts surface started to appear.

6.2 Future work

The loading of our catalysts is relativity low for the current preparation procedure and the performance of the cobalt carbide catalysts were already quite impressive. To further improve the catalyst performance, cobalt loading and preparation conditions would be optimized. First, cobalt loading could be increased to 20% and the catalytic performance evaluation could be conducted to study the influence of the active component loading. The reaction rate is expected to rise with the increasing cobalt loading, but metal is more likely to aggregate and undergoing severer sintering at high temperature.

The performance of the catalysts is strongly depended on the calcination temperature as well as the preparation procedure. Catalysts calcined at different temperature may leads to various oxides. The result carbide carburized from the oxides would also be different which would influence the conversion of CO_2 and selectivity to CH_4. The combination of an optimal calcination temperature with an ideal cobalt loading is expected to further improve the catalytic performance.

Reference

[1] SEM Schematic, Engineering Atoms, University of Cambridge, https://www.eng-atoms.msm.cam.ac.uk/RoyalSocDemos/SEM, 2015.
[2] Terrace4, Transmission electron microscopy, https://en.wikipedia.org/wiki/Transmission_electron_microscopy#, 2019.
[3] D.S. Simakov, Renewable synthetic fuels and chemicals from carbon dioxide: fundamentals, catalysis, design considerations and technological challenges, Springer2017.
[4] M.A. Malik, M.Y. Wani, M.A. Hashim, Microemulsion method: A novel route to synthesize organic and inorganic nanomaterials: 1st Nano Update, Arabian Journal of Chemistry 5 (2012) 397-417.
[5] M. Götz, J. Lefebvre, F. Mörs, A.M. Koch, F. Graf, S. Bajohr, R. Reimert, T. Kolb, Renewable Power-to-Gas: A technological and economic review, Renewable Energy 85 (2016) 1371-1390.
[6] Ontario: Environment profile, Climate Change, Government of Canada, https://www.canada.ca/en/environment-climate-change/corporate/transparency/briefing/ontario-environment-profile.html, 2015.
[7] A. Yatchew, A. Baziliauskas, Ontario feed-in-tariff programs, Energy Policy 39 (2011) 3885-3893.
[8] T.F. Stocker, D. Qin, G.-K. Plattner, M. Tignor, S.K. Allen, J. Boschung, A. Nauels, Y. Xia, V. Bex, P.M. Midgley, Climate change 2013: The physical science basis, Cambridge University Press, 2013.
[9] J. Blunden, 2013 State of the Climate: Carbon dioxide tops 400 ppm, in: D. Hurst (Ed.)https://www.climate.gov/news-features/understanding-climate/2013-state-climate-carbon-dioxide-tops-400-ppm, 2014.
[10] Natural Resources Facts, Natural Resource Canada, https://www.nrcan.gc.ca/energy-facts/natural-gas-facts/20067, 2018.
[11] M. Bailera, P. Lisbona, L.M. Romeo, S. Espatolero, Power to Gas projects review: Lab, pilot and demo plants for storing renewable energy and CO_2, Renewable and Sustainable Energy Reviews 69 (2017) 292-312.
[12] K. Ghaib, K. Nitz, F.Z. Ben - Fares, Chemical methanation of CO_2: a review, ChemBioEng Reviews 3 (2016) 266-275.
[13] M. Younas, L. Loong Kong, M.J. Bashir, H. Nadeem, A. Shehzad, S. Sethupathi, Recent advancements, fundamental challenges, and opportunities in catalytic methanation of CO_2, Energy & Fuels 30 (2016) 8815-8831.
[14] A. Karelovic, P. Ruiz, Mechanistic study of low temperature CO_2 methanation over Rh/TiO_2 catalysts, Journal of Catalysis 301 (2013) 141-153.
[15] Z. Zhang, A. Kladi, X.E. Verykios, Effects of carrier doping on kinetic parameters of CO_2 hydrogenation on supported rhodium catalysts, Journal of Catalysis 148 (1994) 737-747.
[16] J. Xu, Q. Lin, X. Su, H. Duan, H. Geng, Y. Huang, CO_2 methanation over TiO_2–Al_2O_3 binary oxides supported Ru catalysts, Chinese Journal of Chemical Engineering 24 (2016) 140-145.
[17] T. Abe, M. Tanizawa, K. Watanabe, A. Taguchi, CO_2 methanation property of Ru nanoparticle-loaded TiO_2 prepared by a polygonal barrel-sputtering method, Energy & Environmental Science 2 (2009) 315-321.

[18] J.-N. Park, E.W. McFarland, A highly dispersed Pd–Mg/SiO_2 catalyst active for methanation of CO_2, Journal of Catalysis 266 (2009) 92-97.
[19] P. Frontera, A. Macario, M. Ferraro, P. Antonucci, Supported catalysts for CO_2 methanation: a review, Catalysts 7 (2017) 59.
[20] C. Bartholomew, Catalyst deactivation and regeneration, Kirk‐Othmer Encyclopedia of Chemical Technology, 2003.
[21] S. Rahmani, M. Rezaei, F. Meshkani, Preparation of highly active nickel catalysts supported on mesoporous nanocrystalline γ-Al_2O_3 for CO_2 methanation, Journal of Industrial Engineering Chemistry 20 (2014) 1346-1352.
[22] H. Liu, X. Zou, X. Wang, X. Lu, W. Ding, Effect of CeO_2 addition on Ni/Al_2O_3 catalysts for methanation of carbon dioxide with hydrogen, Journal of Natural Gas Chemistry 21 (2012) 703-707.
[23] Y. Yan, Y. Dai, H. He, Y. Yu, Y. Yang, A novel W-doped Ni-Mg mixed oxide catalyst for CO_2 methanation, Applied Catalysis B: Environmental 196 (2016) 108-116.
[24] G. Du, S. Lim, Y. Yang, C. Wang, L. Pfefferle, G.L. Haller, Methanation of carbon dioxide on Ni-incorporated MCM-41 catalysts: The influence of catalyst pretreatment and study of steady-state reaction, Journal of Catalysis 249 (2007) 370-379.
[25] Q. Liu, B. Bian, J. Fan, J. Yang, Cobalt doped Ni based ordered mesoporous catalysts for CO_2 methanation with enhanced catalytic performance, International Journal of Hydrogen Energy 43 (2018) 4893-4901.
[26] W. Li, H. Wang, X. Jiang, J. Zhu, Z. Liu, X. Guo, C. Song, A short review of recent advances in CO_2 hydrogenation to hydrocarbons over heterogeneous catalysts, RSC Advances 8 (2018) 7651-7669.
[27] Y. Yang, L. Jing, X. Yu, D. Yan, M. Gao, Coating aqueous quantum dots with silica via reverse microemulsion method: toward size-controllable and robust fluorescent nanoparticles, Chemistry of Materials 19 (2007) 4123-4128.
[28] S. Vaucher, M. Li, S. Mann, Synthesis of Prussian blue nanoparticles and nanocrystal superlattices in reverse microemulsions, Angewandte Chemie International Edition 39 (2000) 1793-1796.
[29] M. Kishida, K. Umakoshi, J.-i. Ishiyama, H. Nagata, K. Wakabayashi, Hydrogenation of carbon dioxide over metal catalysts prepared using microemulsion, Catalysis Today 29 (1996) 355-359.
[30] A.J. Zarur, J.Y. Ying, Reverse microemulsion synthesis of nanostructured complex oxides for catalytic combustion, Nature 403 (2000) 65.
[31] M. Eckert, Max von Laue and the discovery of X‐ray diffraction in 1912, Annalen der Physik 524 (2012) A83-A85.
[32] A. Monshi, M.R. Foroughi, M.R. Monshi, Modified Scherrer equation to estimate more accurately nano-crystallite size using XRD, World Journal of Nano Science Engineering 2 (2012) 154-160.
[33] D.M. Moore, R.C. Reynolds, X-ray Diffraction and the Identification and Analysis of Clay Minerals, second ed., Oxford university press1989.
[34] R.B. Anderson, Modifications of the Brunauer, Emmett and Teller equation1, Journal of the American Chemical Society 68 (1946) 686-691.

[35] C.D. Doyle, Kinetic analysis of thermogravimetric data, Journal of Applied Polymer Science 5 (1961) 285-292.
[36] B. Stuart, Infrared spectroscopy, Kirk‐Othmer Encyclopedia of Chemical Technology, 2000, pp. 1-18.
[37] J.R. Brownson, C. Lévy-Clément, Nanostructured α-and β-cobalt hydroxide thin films, Electrochimica Acta 54 (2009) 6637-6644.
[38] F. Lyu, Y. Bai, Q. Wang, L. Wang, X. Zhang, Y. Yin, Phase-controllable synthesis of cobalt hydroxide for electrocatalytic oxygen evolution, Dalton Transactions 46 (2017) 10545-10548.
[39] J. Chandradass, M. Balasubramanian, K.H. Kim, Size effect on the magnetic property of $CoAl_2O_4$ nanopowders prepared by reverse micelle processing, Journal of Alloys Compounds 506 (2010) 395-399.
[40] Y. Zhu, H. Li, Y. Koltypin, A. Gedanken, Preparation of nanosized cobalt hydroxides and oxyhydroxide assisted by sonication, Journal of Materials Chemistry 12 (2002) 729-733.
[41] Y. Zhuang, R. Currie, K.B. McAuley, D.S. Simakov, Highly-selective CO2 conversion via reverse water gas shift reaction over the 0.5 wt% Ru-promoted Cu/ZnO/Al2O3 catalyst, Applied Catalysis A: General 575 (2019) 74-86.
[42] L. Xu, J. Zhang, F. Wang, K. Yuan, L. Wang, K. Wu, G. Xu, W. Chen, One-step synthesis of ordered mesoporous $CoAl_2O_4$ spinel-based metal oxides for CO_2 reforming of CH_4, RSC Advances 5 (2015) 48256-48268.
[43] L. Ji, J. Lin, H. Zeng, Metal− support interactions in Co/Al_2O_3 catalysts: a comparative study on reactivity of support, The Journal of Physical Chemistry B 104 (2000) 1783-1790.
[44] J.-H. Kim, B.-R. Son, D.-H. Yoon, K.-T. Hwang, H.-G. Noh, W.-S. Cho, U.-S. Kim, Characterization of blue $CoAl_2O_4$ nano-pigment synthesized by ultrasonic hydrothermal method, Ceramics International 38 (2012) 5707-5712.
[45] G. Kwak, M.H. Woo, S.C. Kang, H.-G. Park, Y.-J. Lee, K.-W. Jun, K.-S. Ha, In situ monitoring during the transition of cobalt carbide to metal state and its application as Fischer–Tropsch catalyst in slurry phase, Journal of Catalysis 307 (2013) 27-36.
[46] B. Sexton, A. Hughes, T. Turney, An XPS and TPR study of the reduction of promoted cobalt-kieselguhr Fischer-Tropsch catalysts, Journal of Catalysis 97 (1986) 390-406.
[47] A.Y. Khodakov, J. Lynch, D. Bazin, B. Rebours, N. Zanier, B. Moisson, P. Chaumette, Reducibility of cobalt species in silica-supported Fischer–Tropsch catalysts, Journal of Catalysis 168 (1997) 16-25.
[48] H.-Y. Lin, Y.-W. Chen, The mechanism of reduction of cobalt by hydrogen, Materials Chemistry Physics 85 (2004) 171-175.
[49] M.-G. Ma, Y.-J. Zhu, Z.-L. Xu, A new route to synthesis of γ-alumina nanorods, Materials Letters 61 (2007) 1812-1815.
[50] J. Quílez‐Pardo, J.J. Solaz‐Portolés, Students' and teachers' misapplication of Le Chatelier's principle: Implications for the teaching of chemical equilibrium, Journal of Research in Science Teaching 32 (1995) 939-957.
[51] J. Baltrusaitis, J. Schuttlefield, E. Zeitler, V.H. Grassian, Carbon dioxide adsorption on oxide nanoparticle surfaces, Chemical Engineering Journal 170 (2011) 471-481.
[52] T. Das, G. Deo, Synthesis, characterization and in situ DRIFTS during the CO_2 hydrogenation reaction over supported cobalt catalysts, Journal of Molecular Catalysis A: Chemical 350 (2011) 75-82.

[53] P. Bera, A.L. Cámara, A. Hornés, A. Martínez-Arias, Comparative in situ DRIFTS-MS study of ^{12}CO-and ^{13}CO-TPR on CuO/CeO_2 catalyst, The Journal of Physical Chemistry C 113 (2009) 10689-10695.
[54] A.M. Turek, I.E. Wachs, E. DeCanio, Acidic properties of alumina-supported metal oxide catalysts: an infrared spectroscopy study, The Journal of Physical Chemistry 96 (1992) 5000-5007.